

Axionlike particle searches in short-baseline liquid scintillator neutrino detectors

D. Aristizabal Sierra^{1,*}, L. Duque^{2,†}, O. Miranda^{2,‡} and H. Nunokawa^{3,§}

¹*Universidad Técnica Federico Santa María - Departamento de Física
Casilla 110-V, Avda. España 1680, Valparaíso, Chile*

²*Departamento de Física, Centro de Investigación y de Estudios Avanzados del IPN,
Apartado Postal 14-740 07000 Mexico, Distrito Federal, Mexico*

³*Pontifícia Universidade Católica do Rio de Janeiro (PUC-Rio) Rua Marques de Sao Vicente,
225, C.P. 38071, 22452-970 Rio de Janeiro, RJ, Brazil*

Short-baseline reactor neutrino experiments using large organic liquid scintillator detectors provide an experimentally rich environment for precise neutrino physics. Neutrino detection is done through inverse beta decay and relies on prompt and delayed signals, which enable powerful background discrimination. In addition to their neutrino program, they offer an ideal experimental environment for other physics searches. Here we discuss the case of axionlike particles (ALPs) produced by either Primakoff-like or Compton-like processes. Their detection relies on the corresponding inverse processes, axio-electric absorption and ALP decays to photon or electron pairs. Assuming experimental parameter values broadly representative of JUNO-TAO or CLOUD we show that scattering ALP processes involve a prompt photon signal component followed by a delayed photon signal about 5 ns after. We point out that if these signals can be resolved, this might allow for efficient ALP signal discrimination against radioactive background. Likewise, coincident events from ALP decays and scintillation light followed by Auger electrons from axio-electric absorption might as well allow for background discrimination. We determine sensitivities in both the nuclear and electron channels using as a benchmark case an experimental setup resembling that of the CLOUD or JUNO-TAO detectors. Our findings demonstrate that with efficient background discrimination these type of technology has the capability to test regions in parameter space not yet explored. In particular, the cosmological triangle can be fully tested and regions of MeV ALP masses with ALP-electron couplings of the order of 10^{-8} can be entirely explored.

Contents

I. Introduction	1
II. ALP production at reactors and detection processes	2
A. ALP production and detection through $g_{\alpha\gamma\gamma}$ couplings	3
B. ALP production and detection through g_{aee} couplings	4
III. ALP signals at JUNO-TAO	5
A. Electron antineutrino detection at JUNO-TAO	5
B. ALP detection at JUNO-TAO	6
1. Inverse Primakoff scattering and ALP decay to photons	6
2. Inverse Compton-like scattering, axio-electric absorption and ALP decay to electron pairs	11
IV. Sensitivities	13
V. Conclusions	15
Acknowledgments	16
A. Fiducial volume ALP decay	16
References	17

I. INTRODUCTION

Axionlike particles (ALPs) are pseudoscalar Nambu-Goldstone bosons that arise from the spontaneous breaking of a global symmetry. They acquire their masses either from small explicitly symmetry-breaking terms or through quantum effects. Examples based on $U(1)$ global symmetries include QCD axions [1–3] and Majoron models [4]. Models involving secluded sectors, related with the origin of dark matter, are as well good examples (see e.g. Ref. [5]). Although these states are light and feebly coupled to Standard Model (SM) fields, they have been subject to intense experimental searches over more than four decades.

ALP scenarios are a general class of models where coupling and mass are not interrelated, in contrast to QCD axion models where couplings are suppressed by the symmetry-breaking scale and thus correlated with the axion mass [6, 7]. Their couplings and masses (m_a) cover wider regions of parameter space and therefore, are testable in a larger class of experiments. In low-mass regions, $m_a \in [10^{-9}, 10^{-4}]$ eV, searches have been carried out in light shining through walls experiments—which rely on photon-axion conversion in external electric or magnetic fields [8–10]—photon polarization experiments that leverage on light dichroism and birefringence effects [11, 12], and fifth force searches including torsion balance tests of the gravitational inverse square law [13].

Soon after the work of Peccei and Quinn and the recognition that such a mechanism implied the existence of a new particle [1, 2], searches using nuclear isotopes de-excitations and reactor facilities were done [14–17]. These measurements were followed up by measurements at TEXONO about 20

*Electronic address: daristizabal@uliege.be

†Electronic address: laura.duque@cinvestav.mx

‡Electronic address: omar.miranda@cinvestav.mx

§Electronic address: nunokawa@puc-rio.br

years ago [18]. Given the nature of these experiments, they are relevant in the low-MeV mass region, in contrast to those mentioned in the previous paragraph.

In this region, astrophysical and cosmological criteria have also played an important role. Production of these states is possible in stellar as well as in supernova environments and at early cosmological times. Thus, if produced at sufficiently high rates, they can potentially disrupt the observed dynamics of such environments [19–25]. Relevant in this region as well are invisible heavy quarkonium decays, along with beam-dump searches and collider experiments [26–31]. The non-observation of deviations above expectations has placed constraints in several spots in parameter space, but in some cases, with a few caveats. In particular, in those spots where astrophysical and cosmological bounds apply [32].

During the last decade or so there has been an increasing interest in ALP searches in different regions of parameter space. The Axion Resonant InterAction Detection Experiment (ARIADNE), leveraging on nuclear magnetic resonance techniques, aims at testing QCD axion models in the $10^{-4} - 10^{-2}$ eV region [33]. The International Axion Observatory (IAXO), a next-generation axion helioscope, will improve upon searches done at CAST [34] in regions of ALP masses up to the order of 1 eV [35]. Current dark matter direct detection experiments are making significant progress as well in the keV to MeV region and will continue improving [36–38]. Forthcoming beam-dump experiments, covering regions of heavier ALP masses, are expected to increase the discovery likelihood. They include SeaQuest [39], MATHUSLA [40], CODEX-b [41], FASER [42] and SHiP [43].

ALP searches using nuclear fission reactors is a subject that recently has been revisited by several authors [44–46]. Studies using nuclear fusion reactors have been as well presented very recently in Ref. [47]. Employing nuclear fission reactors, it has attracted attention mainly because of neutrino detectors suited for coherent elastic neutrino-nucleus scattering measurements (see e.g. [48–50]). The same technology used for such applications can also be used for ALP and dark photon searches at no extra cost. The ALP search capabilities of a satellite experiment of the Jiangmen Underground Neutrino Observatory (JUNO) [51, 52], the Taishan Antineutrino Observatory (JUNO-TAO) [53], have been already studied in Ref. [54], using ALP-electron scattering processes. Recently as well the NEON experiment and the MINER collaboration have reported upon their searches [55, 56]. Although using different detection technologies compared to those used by the JUNO-TAO experiment, these results demonstrate the potential of this type of searches.

In this paper, we claim that upcoming short-baseline neutrino experiments relying on large organic liquid scintillator detectors—such as JUNO-TAO [53] or CLOUD [57]—might contribute to the global ALP search program. In order to do so, we consider a JUNO-TAO-like detector concept with parameter specifications as described in Ref. [53]. For the sake of readability, from here on we refer to this detector configuration simply as JUNO-TAO. For reasons to be discussed in Sec. II, we focus our analysis on ALP couplings to nuclei and electrons. These couplings induce scattering and decay

processes, with the latter dominating the “high” ALP mass region. Thus, their inclusion increases the discovery potential. The JUNO-TAO detector relies on scintillation light, which nuclear recoils produce little. We argue that if scintillation light—along with final-state photons produced in the scattering process itself—can be recorded over a large enough window time (one minute or so) an enhancement of the signal might be possible.

We show as well that both nuclear and electron recoils produce a prompt and a delayed photon signal, which we argue can potentially be used for background discrimination. And identify the type of coincident event signals ALP decays lead to. We demonstrate that taking advantage of potential background discrimination, JUNO-TAO might have the capabilities to test regions in the ALP parameter space where either caveats apply or which have not been yet explored. Our analysis is, therefore, complementary to the findings provided in Ref. [54].

The remainder of this paper is organized as follows. In Sec. II, we provide a discussion of differential scattering cross sections, decay widths, and survival and decay probabilities. We present results that allow the calculation of ALP fluxes and differential event rates. In Sec. III, we start with a brief overview of neutrino detection at JUNO-TAO, which serves as a *frame* for the analysis of scattering ALP signals in nuclear and electron recoils. We show that ALP signatures imply a prompt and a delayed photon component if arising from scattering or coincident photon event signals if generated by ALP decays. In Sec. IV, we present results for sensitivities in both cases, nuclear and electron recoils. Finally, in Sec. V we summarize and present our conclusions. Details of a two-dimensional model for the determination of the most likely ALP decay point within the detector fiducial volume are presented in App. A.

II. ALP PRODUCTION AT REACTORS AND DETECTION PROCESSES

From a phenomenological point of view production of ALPs in reactors and their further detection depends on whether they couple to photons, electrons or quarks. Coupling to photons, controlled by the dimensionful coupling $g_{\alpha\gamma\gamma}$, allow production through Primakoff-like scattering and detection through the corresponding inverse process. It enables as well ALP decay to photon pairs. Primakoff-like processes follow from the standard Primakoff effect, where photon-nucleus scattering produces neutral pions.

Coupling to electrons, in this case controlled by the dimensionless coupling g_{aee} , involve a richer phenomenology. Production goes through Compton-like processes, while detection through the inverse process or axio-electric absorption (analogous to photo-electric absorption). It can generate ALP decays to e^+e^- pairs, in kinematically allowed regions.

Couplings to quarks imply couplings to nucleons, dictated by the dimensionless coupling g_{ann} . Production can proceed through different avenues. For instance, heavy isotopes undergoing either α or β^+ decay produce excited nuclear iso-

topes that through de-excitation will produce monoenergetic ALPs from magnetic multipole transitions (ALPs are parity odd pseudoscalars, $J^P = 0^-$). Detection will happen through nuclear resonant absorption, which will be scarce. The reason being that the flux of monoenergetic ALPs follow from nuclear de-excitations of a large variety of nuclear isotopes, of which carbon—the main material target in the JUNO-TAO detector—contributes only to a small fraction¹. And monoenergetic ALPs that do not match the nuclear energy gaps of the carbon nucleus are very unlikely to get absorbed.

Scenarios where production proceeds through g_{ann} couplings, thus, typically require an extra coupling for detection. For instance, pioneer searches at the Bugey reactor in the 80's relied on ALP decays to photon pairs [15]. Analysis of these type of models—therefore—demand going beyond minimality, defined as scenarios where only one coupling is present at a time. Here we then focus only on ALP models where the ALP couples either to photons or electrons.

A. ALP production and detection through $g_{a\gamma\gamma}$ couplings

Photon interaction in the electromagnetic (EM) field of nuclei produce an ALP flux through the t -channel $\gamma + N \rightarrow a + N$ process. Its intensity depends on the photon flux and the ALP-photon conversion cross section, which for scattering in a nucleus with atomic number Z reads [59]

$$\frac{d\sigma_a^P}{dt} = 2\alpha Z^2 F^2(t) g_{a\gamma\gamma}^2 \frac{m_N^4}{t^2(m_N^2 - s)^2(t - 4m_N^2)^2} G(t, s). \quad (1)$$

Here α is the fine structure constant, $F(t)$ is a form factor that accounts for electron cloud screening effects, which are relevant for ALP energies of the order of a few eV, s and t are the Mandelstam variables, and m_N is the nucleus mass. Thus, for the energy range we are interested here ($E_a \gtrsim m_e$, where E_a and m_e are, respectively, ALP energy and electron mass) ALPs scatter off the nucleus with no intervention by the electron cloud. Note that because of the kinematic cut $E_a \lesssim 10$ MeV, nuclear form factor effects have no significant impact. The differential cross section in Eq. (1), therefore, can be safely evaluated in the limit $F(t) \rightarrow 1$. Furthermore, the kinematic function $G(t, s)$ reads

$$G(t, s) = m_a^2 t (m_N^2 + s) - m_a^4 m_N^2 - t [(m_N - s)^2 + st]. \quad (2)$$

The reactor differential photon flux $d\Phi_\gamma/dE_\gamma$ (E_γ being the photon energy) involves a continuous component that follows from electron Bremsstrahlung, Compton scattering and electron-positron pair annihilation². It involves as well a host of spectral lines that come from the de-excitation of the different isotopes fission yields. Since we focus our analysis on

ALP couplings to either photons or electrons, here we consider only the continuous component which is well described by a power-law spectrum [60].

ALPs produced in the reactor core propagate isotropically. For a detector placed at a baseline L , ALPs with lifetimes larger than $L(E_a/|\vec{p}_a|)$ (\vec{p}_a being the ALP momentum) have a non-zero probability of interacting with the target material. Since the ALP lifetime is determined by $g_{a\gamma\gamma}$ and m_a (see below), in some regions of parameter space the flux will be diminished. This is accounted for by the survival probability

$$\mathcal{P}_{\text{Surv}} = e^{-L/\ell_a} = e^{-L/(v_a\tau_a)} = e^{-LE_a/(|\vec{p}_a|\tau_a)}, \quad (3)$$

where $\tau_a = \Gamma_a^{-1}$ refers to the ALP lifetime and Γ_a to its total decay width

$$\Gamma(a \rightarrow \gamma\gamma) = g_{a\gamma\gamma}^2 \frac{m_a^3}{64\pi}. \quad (4)$$

The differential cross section in Eq. (1) is sharply peaked, as can be seen by noticing that $|t|/m_N^2 = 2E_r/m_N \ll 1$ (with E_r the nucleus recoil energy) and so scattering produces forward scattered ALPs. This observation allows for the following simplification

$$\frac{d\sigma_a^P}{dE_a} = \sigma_a^P(E_a)\delta(E_a - E_\gamma), \quad (5)$$

where the total cross section is obtained from integration of Eq. (1). As any flux, the ALP flux follows from a convolution over photon energies of the differential cross section in Eq. (5) and the continuous photon flux. However, the sharp peak structure of the differential cross section allows for a simplified expression of the ALP flux [45]

$$\frac{d\Phi_a^P}{dE_a} = \mathcal{P}_{\text{Surv}} \frac{\sigma_a^P}{\sigma_{\text{Tot}}} \left. \frac{d\Phi_\gamma}{dE_\gamma} \right|_{E_\gamma=E_a}. \quad (6)$$

Here $\sigma_{\text{Tot}} = \sigma_{\text{SM}} + \sigma_a^P$, with σ_{SM} involving all possible EM processes with an initial-state photon: Compton scattering, Rayleigh scattering, photo-electric absorption and electron-pair production in the field of the nucleus and the electron [61]. It is worth pointing out that the differential cross section-to-total cross section ratio “measures” the amount of photons which undergo ALP conversion. It can be understood as a branching ratio equivalent. Furthermore, for $g_{a\gamma\gamma} \lesssim 10^{-3} \text{ GeV}^{-1}$ (the ALP coupling parameter space region of interest) the SM cross section exceeds the Primakoff cross section by several orders of magnitude. The non-standard contribution can then be safely neglected.

Detection proceeds through inverse Primakoff (IP) scattering ($a + N \rightarrow \gamma + N$) and ALP decay (D). The differential event rate can then be written as

$$\left. \frac{dN}{dE_a} \right|_{\text{Total}} = \left. \frac{dN}{dE_a} \right|_{\text{IP}} + \left. \frac{dN}{dE_a} \right|_{\text{D}}. \quad (7)$$

Since the inverse Primakoff differential cross section matches that of Primakoff scattering—Eq. (5)—up to a factor 2 [45],

¹ The cumulative fission yields of ²³⁵U and ²⁴¹Pu include carbon along with other 57 and 54 nuclear isotopes, respectively [58].

² Because of the relative direction of the initial-state positron and final-state photon, the would-be 511 keV spectral line broaden (see Sec. III A for details).

the first term in Eq. (7) can be simplified in the same way the ALP photon flux has been. Explicitly both terms read

$$\left. \frac{dN}{dE_a} \right|_{\text{IP}} = \frac{m_{\text{det}}}{2\pi L^2} N_A \sum_{i=\text{H,C}} \frac{f_i^n}{m_{\text{molar}}^i} \sigma_{a,i}^{\text{P}} \left. \frac{d\Phi_a^{\text{P}}}{dE_a} \right|_{\text{U}}, \quad (8)$$

$$\left. \frac{dN}{dE_a} \right|_{\text{D}} = \mathcal{P}_{\text{Decay}} \frac{A}{4\pi L^2} \left. \frac{d\Phi_a^{\text{P}}}{dE_a} \right|_{\text{U}}, \quad (9)$$

where m_{det} is the detector mass, N_A is the Avogadro number, m_{molar} is the target nuclei molar mass and A is the detector transverse area (see below). The JUNO-TAO detector is filled with linear alkylbenzene, LAB in short. Thus, f_i^n refers to the hydrogen and carbon LAB mass fractions [see Eq. (52) and the discussion thereof as well as Sec. III A]. In both cases the ALP flux is calculated by assuming photon production in uranium. For m_{det} we employ 1 tonne [53]. Note that the differential event rate in decays involves the probability of decay within the detector fiducial volume as well as its transverse area $A = \pi R_{\text{JUNO-TAO}}^2$ ($R_{\text{JUNO-TAO}} = 0.65\text{m}$ is the JUNO-TAO detector fiducial volume radius). The former is given by

$$\mathcal{P}_{\text{Decay}} = 1 - e^{-rE_a/(\bar{p}_a\tau_a)}, \quad (10)$$

where r refers to the most likely depth where decay might take place. Note as well that the decay probability increases with increasing ALP mass, so expectations are that decays become relevant at higher ALP masses despite the process not having a kinematic threshold. Of course integration of the total differential event rate over ALP energies, in the range $[m_e, 10\text{MeV}]$, determines the number of events for a given point in parameter space.

B. ALP production and detection through g_{aee} couplings

ALP production in scenarios where the ALP couples to electrons is determined by the following differential cross section [62]

$$\frac{d\sigma_a^{\text{C}}}{dE_a} = \frac{Z\alpha x}{4(s-m_e^2)(1-x)E_\gamma} g_{aee}^2 G(x), \quad (11)$$

where the kinematic function $G(x)$ reads

$$G(x) = x - \frac{2m_a^2 s}{(s-m_e^2)^2} + \frac{2m_a^2}{(s-m_e^2)^2} \left(\frac{m_e^2}{1-x} + \frac{m_a^2}{x} \right). \quad (12)$$

In the electron rest frame, $s = m_e^2 + 2E_\gamma m_e$ and

$$x = 1 - \frac{E_a}{E_\gamma} + \frac{m_a^2}{2E_\gamma m_e}. \quad (13)$$

The ALP flux follows as well from a convolution of the differential cross section in Eq. (11), normalized to $\sigma_{\text{Tot}} = \sigma_{\text{SM}} + \sigma_a^{\text{C}}$, and the continuous photon flux. It reads

$$\left. \frac{d\Phi_a^{\text{C}}}{dE_a} \right|_{\text{U}} = \mathcal{P}_{\text{Surv}} \int_{E_\gamma^{\text{min}}}^{E_\gamma^{\text{max}}} \frac{1}{\sigma_{\text{Tot}}} \frac{d\sigma_a^{\text{C}}}{dE_a} \frac{d\Phi_\gamma}{dE_\gamma} dE_\gamma. \quad (14)$$

The integration upper limit is determined by kinematic constraints, $E_\gamma^{\text{max}} = 10\text{MeV}$, and $E_\gamma^{\text{min}} = (m_a m_e - m_a^2/2)/(m_e - m_a)$. The latter follows from the $2 \rightarrow 2$ scattering process kinematics. Here—as in the case of ALPs coupled to light— $\sigma_{\text{SM}} \gg \sigma_a^{\text{C}}$ in the regions of parameter space of interest. Note that the flux is as well weighted by the survival probability, but in this case the ALP decay length is determined by the conditions dictated by the ALP decay mode $a \rightarrow e^+e^-$ for which the width reads

$$\Gamma(a \rightarrow e^+e^-) = \frac{m_a g_{aee}^2}{8\pi} \sqrt{1 - 4\frac{m_e^2}{m_a^2}}. \quad (15)$$

As we have pointed out, detection proceeds through inverse Compton-like (IC) scattering, axio-electric absorption (A) and decay (D). The total differential event rate thus reads

$$\left. \frac{dN}{dE_a} \right|_{\text{Total}} = \left. \frac{dN}{dE_a} \right|_{\text{IC}} + \left. \frac{dN}{dE_a} \right|_{\text{A}} + \left. \frac{dN}{dE_a} \right|_{\text{D}}. \quad (16)$$

For a detector deployed at a distance L from the reactor core, the different contributions are given by [45]

$$\left. \frac{dN}{dE_\gamma} \right|_{\text{IC}} = \frac{m_{\text{det}}}{4\pi L^2} N_A \sum_{i=\text{H,C}} Z_i \frac{f_i^n}{m_{\text{molar}}^i} \int_{E_a^{\text{min}}}^{E_a^{\text{max}}} \left. \frac{d\sigma_a^{\text{IC}}}{dE_\gamma} \right|_{Z=1} \left. \frac{d\Phi_a^{\text{C}}}{dE_a} \right|_{\text{U}} dE_a, \quad (17)$$

$$\left. \frac{dN}{dE_a} \right|_{\text{A}} = \frac{m_{\text{det}}}{4\pi L^2} N_A \sum_{i=\text{H,C}} \frac{f_i^n}{m_{\text{molar}}^i} \sigma_{\text{A}}^i \left. \frac{d\Phi_a^{\text{C}}}{dE_a} \right|_{\text{U}}, \quad (18)$$

$$\left. \frac{dN}{dE_a} \right|_{\text{D}} = \frac{A}{4\pi L^2} \mathcal{P}_{\text{Decay}} \left. \frac{d\Phi_a^{\text{C}}}{dE_a} \right|_{\text{U}}. \quad (19)$$

The decay probability in Eq. (19) follows Eq. (10), but in this case the decay lifetime is calculated from the ALP de-

cay mode $a \rightarrow e^+e^-$. Here, we have written the differential event rate for the inverse Compton-like process in terms of

the final-state photon energy. For the corresponding expression in terms of the initial-state ALP energy, one can write $dN/dE_a|_{\text{IC}} = |dE_\gamma/dE_a| dN/dE_\gamma|_{\text{IC}}$, with the Jacobian determined by the constraints implied by the kinematics of the $2 \rightarrow 2$ scattering process

$$E_\gamma = \frac{y}{2(m_e + E_a - |\vec{p}_a| \cos \theta)}, \quad (20)$$

where $y = 2m_e E_a + m_a^2$ and θ is the angle between the incoming ALP and outgoing photon trajectories. The lower integration limit in Eq. (17) follows from Eq. (20) by solving for

E_a with $\theta = 0$ (and so $E_\gamma^{\text{max}} = 10$ MeV). The upper limit, instead, from Eq. (13) by solving for E_a and noting that E_a is maximized for $E_\gamma = E_\gamma^{\text{max}}$ and $x = x_{\text{min}}$. The latter given by [63]

$$x_{\text{min}} = \frac{1}{2s} \left[(s - m_e^2 + m_a^2) - \sqrt{(s - m_e^2 + m_a^2)^2 - 4m_a^2 s} \right]. \quad (21)$$

The inverse Compton-like differential cross section and the axio-electric absorption cross section read [64, 65]

$$\frac{d\sigma_a^{\text{IC}}}{dE_\gamma} = \frac{Z\alpha g_{aee}^2}{32\pi} \frac{y}{m_e^2 |\vec{p}_a|^2 E_\gamma} \left(1 + \frac{4m_e^2 E_\gamma^2}{y^2} - \frac{4m_e E_\gamma}{y} - \frac{4m_a^2 m_e |\vec{p}_a|^2 E_\gamma}{y^3} \sin^2 \theta \right), \quad (22)$$

$$\sigma_A = \frac{g_{aee}^2}{|\vec{\beta}|} \frac{3E_a^2}{16\pi\alpha m_e^2} \left(1 - \frac{|\vec{\beta}|^{2/3}}{3} \right) \sigma_{\text{PE}}(E_a). \quad (23)$$

Here θ is obtained from the kinematic constraints implied by Eq. (20), $|\vec{\beta}|$ is the ALP rapidity and $\sigma_{\text{PE}}(E_a)$ is the SM photoelectric absorption total cross section evaluated at ALP energies.

The results presented in this section, along with those from Sec. II A, allow the determination of ALP event rates. There are, however, a couple of questions that still have not been addressed. First of all, how do signals at the JUNO-TAO detector look like. Secondly, up to which degree these signals can be identified and separated from background. The latter comes from different sources—including neutrino scattering events—but of which the most abundant are singles from radioactivity that amount to about 3×10^9 events/year [53]. In what follows, then, we aim to determine how the signals actually look like and whether their features enable their identification above background. We want to stress that the analysis is only aimed at providing a first approach to the most general problem. A more realistic and precise determination very likely calls for a full Geant4 detector simulation.

III. ALP SIGNALS AT JUNO-TAO

To determine more precisely the type of ALP signals expected at JUNO-TAO, we rely on the same strategy employed for neutrino detection. We take advantage of the final-state photon produced in either inverse Primakoff or inverse Compton-like processes, on which detection is based upon. Thus, we first review neutrino detection at JUNO-TAO and then proceed with ALP signals.

A. Electron antineutrino detection at JUNO-TAO

Electron anti-neutrinos produced at the Taishan Nuclear Power Plant are detected through inverse β decay (IBD) processes:

$$\bar{\nu}_e + p^+ \rightarrow n^0 + e^+. \quad (24)$$

The final-state products produce two distinctive γ signals, as we now discuss [66]. In the proton rest frame, energy conservation implies:

$$E_{\bar{\nu}_e} = m_n - m_p + m_e + T_n + T_{e^+}, \quad (25)$$

where T_n and T_{e^+} are, respectively, the neutron and positron kinetic energies. From Eq. (25) one can see that at threshold ($T_n = T_{e^+} = 0$) IBD will happen provided $E_{\bar{\nu}_e} \geq E_{\bar{\nu}_e}^{\text{Th}} = 1.804$ MeV. For electron-positron pair annihilation into $\gamma_1 + \gamma_2$:

$$e^+(p_{e^+}) + e^-(p_{e^-}) \rightarrow \gamma_1(p_\gamma) + \gamma_2(p'_\gamma), \quad (26)$$

energy and momentum conservation (in the electron reference frame) implies

$$T_{e^+} + 2m_e = E'_\gamma + E_\gamma, \quad (27)$$

$$\vec{p}_{e^+} = \vec{p}_\gamma + \vec{p}'_\gamma. \quad (28)$$

At threshold, this means that pair annihilation produces back-to-back monochromatic photons with $E_\gamma = E'_\gamma = m_e = 511$ keV, i.e. monochromatic lines at $\lambda = 2.4$ pm. For neutrinos above threshold ($T_{e^+} \neq 0$), photon energies become angu-

lar dependent

$$E_\gamma = \frac{m_e(T_{e^+} + 2m_e)}{T_{e^+} + 2m_e - |\vec{p}_{e^+}| \cos \theta}, \quad (29)$$

$$E'_\gamma = \frac{(T_{e^+} + 2m_e)(T_{e^+} + m_e - |\vec{p}_{e^+}| \cos \theta)}{T_{e^+} + 2m_e - |\vec{p}_{e^+}| \cos \theta}. \quad (30)$$

Here θ refers to the angle between the incoming positron and one of the outgoing photons (γ_1). From Eqs. (29) and (30) one can see that when γ_1 scatters along the incoming positron direction [forward scattering ($\theta = 0$)] $E_\gamma = E_\gamma^{\text{Max}}$ and so $E'_\gamma = E_\gamma^{\text{Min}}$. Conversely, when γ_1 scatters opposite to the incoming positron direction [backward scattering ($\theta = \pi$)] $E_\gamma = E_\gamma^{\text{Min}}$ and so $E'_\gamma = E_\gamma^{\text{Max}}$. Thus, the angular dependence leads to photon energy distributions that range from E_γ^{Min} to E_γ^{Max} .

Assuming different incoming electron anti-neutrino energies and 10^4 scattering events, we have randomly sampled Eqs. (29) and (30) over $\theta \in [0, \pi]$. With the results of such sampling, we have then determined the photon energy probability density functions (PDFs) for both γ_1 and γ_2 . Results are displayed in Fig. 1. For γ_1 (left graph) one can see that most events tend to cluster towards small energy bins. This means that most of those photons are produced opposite to the incoming positron direction. In contrast—and as expected—the other final-state photons (γ_2) clump towards the highest energy bins, in agreement with our previous discussion (see the right graph of Fig. 1). Note that these do not reflect the event rate angular PDFs, whose calculation requires the electron-positron annihilation differential cross section. They are just photon energy PDFs derived from simple kinematic criteria, to give an approximate qualitative illustration. Despite these scattering events taking place above threshold, final-state photons are still back-to-back. Momentum conservation in Eq. (28) implies

$$\sin \alpha = \frac{E_\gamma}{E'_\gamma} \sin \theta, \quad (31)$$

where α measures the direction of the incoming positron and γ_2 . Thus, taking the case of those events for which $E_\gamma = E_\gamma^{\text{Min}}$, Eq. (31) shows that $\alpha = 0$.

The photon signal from the final-state neutron proceeds in a different way. The JUNO-TAO detector uses LAB, a liquid scintillator organic compound with chemical composition $C_6H_5C_nH_{2n+1}$ (with $n \in [10, 16]$) [53, 67]. LAB-based scintillators have been extensively used in neutrino detection in the last 15 years or so, Daya Bay along with RENO and COSINE-100 are clear examples [68–70]. JUNO-TAO and JUNO as well thus leverage on this expertise. Although the bulk of the liquid scintillator is LAB, it comprises as well small fractions of other compounds: (i) A gadolinium mass fraction of 0.1%, (ii) a fluorescent agent (2.5-Diphenyloxazole, PPO, $C_{15}H_{11}NO$) concentration of 2 g/L, (iii) a wavelength shifter (Bis-MSB, $C_{24}H_{22}$) concentration of 1 mg/L, (iv) a co-solvent of 0.05% ethanol (C_2H_6O) [53].

Of particular relevance for electron anti-neutrino detection is the Gd doping. Gd has seven stable isotopes, of which five

have relative abundances in the 15% – 25% range. Furthermore it has the largest neutron absorption cross section among natural stable isotopes, with ^{155}Gd and ^{157}Gd exhibiting the largest cross sections [71]:

$$\begin{aligned} ^{155}\text{Gd}(n, \gamma) : \quad \sigma &= 60740.2 \text{ barn}, \\ ^{157}\text{Gd}(n, \gamma) : \quad \sigma &= 253765.6 \text{ barn}. \end{aligned} \quad (32)$$

Thus, neutrons produced in IBD are captured predominantly by ^{155}Gd and ^{157}Gd . Neutron capture produces either ^{156}Gd or ^{158}Gd excited isotopes which then cascade decay to their ground state through the emission of multiple photons. The de-excitation process is a complex one, however the overall energy of the emitted photons is fixed by the Q value of the nuclear reaction (neutron binding energy):

$$\begin{aligned} ^{155}\text{Gd} + n^0 &\rightarrow ^{155}\text{Gd}^* \rightarrow ^{156}\text{Gd} + \sum_i \gamma_i \quad (Q = 8.536 \text{ MeV}), \\ ^{157}\text{Gd} + n^0 &\rightarrow ^{157}\text{Gd}^* \rightarrow ^{158}\text{Gd} + \sum_i \gamma_i \quad (Q = 7.937 \text{ MeV}). \end{aligned} \quad (33)$$

Photons produced in the cascade thus produce a second scintillation light signal that enables the identification of the IBD signal above background. For a 0.1% Gd-doped LAB, the average neutron capture time is $\sim 30 \mu\text{s}$ [53, 66]. Thus, the prompt scintillation signal from pair annihilation combined with the delayed scintillation signal from neutron capture allows for an efficient reconstruction of electron antineutrino events.

B. ALP detection at JUNO-TAO

Leveraging on the same strategy used for neutrino detection, here we aim at showing that ALP detection features as well prompt and delayed photon signals. That this is the case is somewhat expected. Both inverse Primakoff and inverse Compton-like scattering produce a final-state photon. So, interactions produce a prompt scintillation signal from the final-state photon and a delayed one from ionization produced by nuclear or electron recoil. In what follows, we characterize both signals and determine their time delay.

To estimate the scintillation light produced in nuclear or electron recoils, two quantities are required: (i) A representative photon yield, (ii) a typical photon emission spectrum. The photoelectron yield is about 4500 per MeV. Since photodetection efficiency (PDE) peaks at 50%, this means that about 9000 photons per MeV are produced [53]. The emission spectrum is dominated by the wavelength shifter BisMSB and peaks at 430 nm, right where the PDE peaks as well (see e.g. [67]).

1. Inverse Primakoff scattering and ALP decay to photons

Starting with *Primakoff scattering*—and so nuclear recoils—the light yield can be calculated with the aid of Birks'

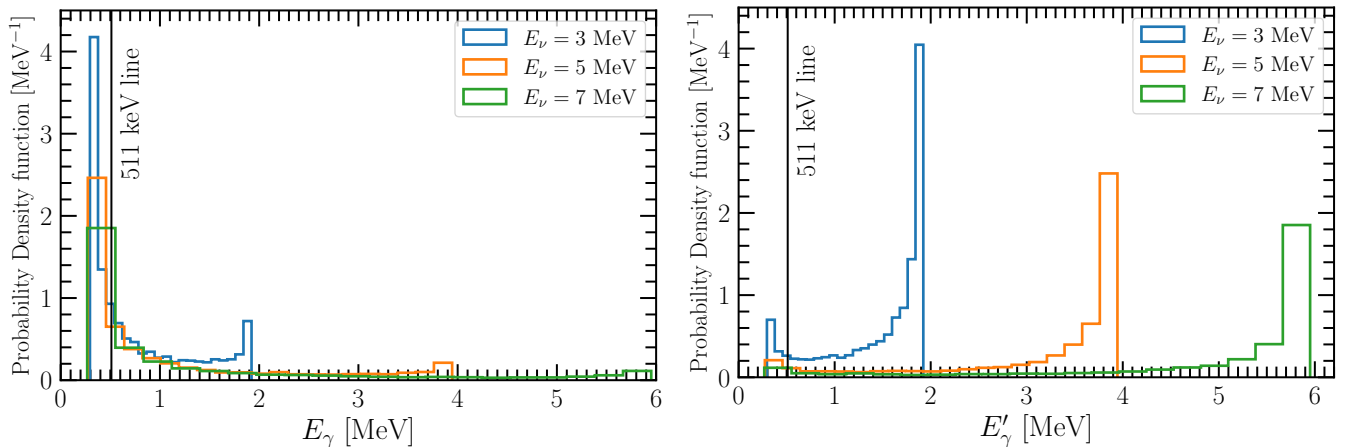


FIG. 1: Photon energy probability distribution functions (PDFs) in pair annihilation for representative electron antineutrino energies (all of them substantially above threshold) for γ_1 (left graph) and γ_2 (right graph). These results are based on random sampling of the kinematic relations shown in Eqs. (29) and (30). For the PDFs 10^4 scattering events and 20 energy bins have been assumed. The latter assuming a $\Delta E_\gamma \simeq 8$ keV photon energy resolution. Back-to-back photons cluster towards low and high energy bins.

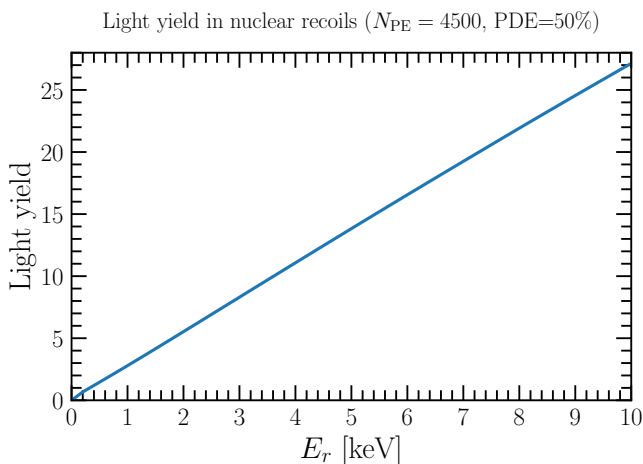


FIG. 2: Estimated light yield—produced in a single nuclear recoil—as a function of nuclear recoil energy. We use 4500 photoelectrons per MeV (9 photons per keV) as a proxy and a PDE of 50% [53].

law [72]

$$L_{\text{yield}}(E_r) = \frac{E_r}{1 + k_B^{\text{Eff}} E_r} Y. \quad (34)$$

Here Y refers to a proxy light yield for which we use $Y = 9$ photons/keV and $k_B^{\text{Eff}} = k_B/\ell$ is an effective Birks' constant (Birks' constant per particle path length, ℓ). Note that in reality Eq. (34) follows from Birks' law after integration over particle path, assuming that energy loss per unit length is proportional to energy. For Birks' constant we have $\rho k_B \subset [1, 5] \times 10^{-3} \text{ g/cm}^2/\text{MeV}$ [73], so taking $\rho_{\text{LAB}} = 863 \times 10^{-3} \text{ g/cm}^3$ we find

$$k_B \subset [1.16, 5.79] \times 10^{-3} \frac{\text{cm}}{\text{MeV}}. \quad (35)$$

Calculation of k_B^{Eff} requires a particle path length (a function of particle energy). We have adopted the particle length of alpha particles in plastic scintillator (vinyltoluene-based) [74], which, to a certain degree, resembles LAB. Fig. 2 shows the estimated light yield per nuclear recoil as a function of nuclear recoil energy.

As expected, large light yields demand high recoil energies, which are by default small for the ALP energies involved: From the kinematics of the inverse Primakoff process, one finds

$$E_\gamma = \frac{m_a^2 + 2E_a m_N}{2[(E_a + m_N) - |\vec{p}_a| \cos \theta]}, \quad (36)$$

where in this case θ refers to the angle between the trajectory of the incoming ALP and the trajectory of the outgoing photon. From this expression—in the limit $m_a < E_a \ll m_N$ —one finds

$$E_r = E_a - E_\gamma \simeq \frac{E_a^2}{m_N} (1 - \cos \theta) \subset \frac{E_a^2}{m_N} [0, 2], \quad (37)$$

which shows that $E_r \simeq O(\text{keV})$. One can see that maximization of E_r requires backward photon scattering, which is unlikely because of the initial-state momentum and the mass of the scatterers in LAB (mainly carbon nuclei). Indeed it is the other way around, as one can check from the constraints implied by momentum conservation. In the limit $E_r \ll E_a$, the angle between the incoming ALP and the outgoing photon can be written as

$$\cos \theta \simeq 1 - \frac{m_N E_r}{E_a^2} + \frac{E_r}{E_a}. \quad (38)$$

This demonstrates that inverse Primakoff processes produce predominantly forward photon scattering, as we have already argued based on the differential cross section in Eq. (1). Recoil energies, therefore, are expected to cluster towards the lower side of the energy interval in Eq. (37).

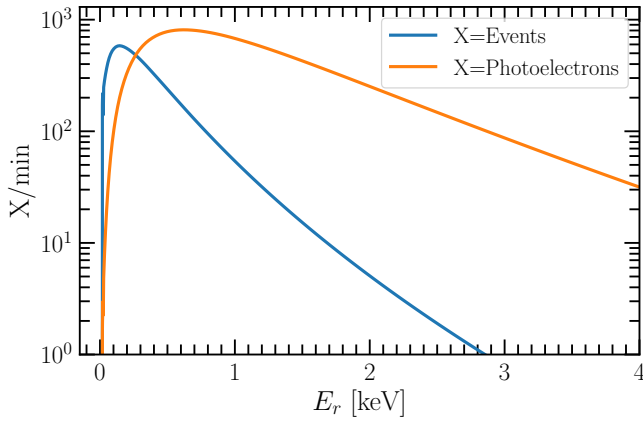


FIG. 3: Event rate per minute as well as number of PEs in detection through inverse Primakoff scattering as a function of nuclear recoil energy. A point in parameter space within the cosmological triangle has been used (see text for more details): $m_a = 0.3 \text{ MeV}$ and $g_{a\gamma\gamma} = 9.5 \times 10^{-3} \text{ GeV}^{-1}$.

In principle, however, this does not mean that the photon yield produced in nuclear recoils is not observable. The point here is that within a given time interval, say Δt , a certain amount of events at fixed recoil energies will take place. So, despite the small light yield produced in a single nuclear recoil event the overall light yield over Δt may be potentially large enough for the signal to be recorded. Fig. 3 shows the expected event rate per minute for a point in parameter space within the cosmological triangle (see Sec. IV for details) corresponding to $m_a = 0.3 \text{ MeV}$ and $g_{a\gamma\gamma} = 9.5 \times 10^{-3} \text{ GeV}^{-1}$. This result shows that up to $\sim 2 \text{ keV}$ events are abundant, thus enhancing the intensity of the scintillation light signal and so of the PE rate.

With the number of events at hand, the number of photons produced in Δt can be calculated according to $N_\gamma/\Delta t = (\text{Events}/\Delta t) \times L_{\text{yield}}$. The intensity of the signal in Δt can then be cast as follows

$$I = \left(\frac{N_\gamma \times L_{\text{yield}}}{10} \right) \left(\frac{\text{min}}{\Delta t} \right) \left(\frac{E_r}{\text{MeV}} \right) \left(\frac{10 \text{ m}^2}{A} \right) \frac{\text{MeV}}{\text{m}^2 \text{ min}}. \quad (39)$$

Note that here we have taken 10 m^2 as the total area covered by the silicon photo-multipliers [75]. The intensity combined with the PE-per-MeV proxy ($N_{\text{PE}} = 4500 \text{ PE/MeV}$) allows the determination of the photoelectron rate, $N_{\text{PE}}^M = I \times A \times N_{\text{PE}}$. Fig. 3 shows the result as a function of nuclear recoil energy. It demonstrates that if the number of photoelectrons over—say—1 min can be recorded/identified, nuclear recoil events might be observable in certain regions of parameter space. For this to be the case, however, the scintillation light spectrum should be characterized.

As we have already stressed, a full characterization of the nuclear recoil scintillation light spectrum requires an emission spectrum proxy. A characterization of the BisMSB emission spectrum shows two peaks, with the dominant peak at $\lambda = 430 \text{ nm}$ (see e.g. [67]). Although available, we have instead restored to a Gaussian function parametrization with

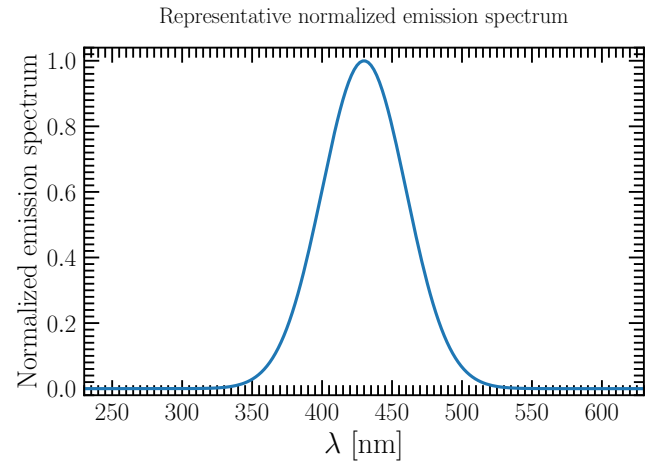


FIG. 4: Normalized Gaussian function (by setting $I_0 = 1$ in Eq. 40) with $\mu = 430 \text{ nm}$ as a representative photon emission spectrum for the JUNO-TAO cocktail.

mean $\lambda_0 = 430 \text{ nm}$ and standard deviation $\sigma = 30 \text{ nm}$. Thus, for the emission spectrum intensity (normalized to an arbitrary reference intensity I_0 at $\lambda = \lambda_0$) we write

$$I(\lambda) = I_0 e^{-\left(\frac{\lambda - \lambda_0}{\sqrt{2}\sigma}\right)^2}. \quad (40)$$

Fig. 4 shows the result we have relied upon in the determination of the nuclear recoil scintillation light emission spectrum PDF. Note that although used for practical purposes, it resembles closely the measured spectrum.

We proceed then as follows. A recoiling nucleus produces excitation of the surrounding medium, which, through de-excitation processes produce scintillation light (photons). The amount of photons is determined by Eq. (34) and their wavelengths by the range dictated by the emission spectrum in Fig. 4, $[350, 500] \text{ nm}$. We then determine the statistical weight of the wavelengths within that range by generating a set containing $N_\lambda = 5000$ values and calculating their discrete probability distribution

$$\mathcal{P}_i = \frac{I(\lambda_i)}{\sum_{j=1}^{N_\lambda} I(\lambda_j)}. \quad (41)$$

For fixed recoil energies, we then randomly sample from the distribution in Eq. (41) as many wavelengths as photons produced in Δt . Fig. 5 (left graph) shows the result for three recoil energy choices (see Tab. I), for the same parameter space point used in the generation of the event spectrum in Fig. 3. As expected, the scintillation light spectrum produced in nuclear recoils follows closely the emission spectrum proxy (peaking around 430 nm). Thus, spectra of this type with a relatively small number of photoelectrons recorded over a sizable time interval—for instance 1 min—could be hinting towards ALP signals induced by Primakoff scattering. Of course, radioactive processes are very likely capable of inducing this type of signals as well (see e.g. Ref. [75]). So the question is whether they can be disentangled from the actual signals.

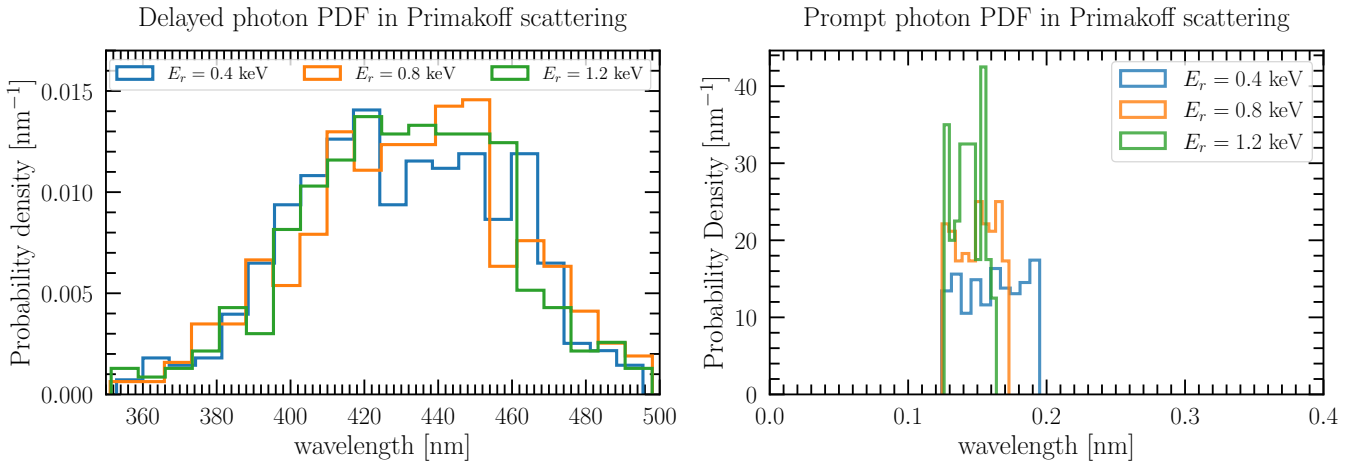


FIG. 5: **Left graph:** Probability distribution function as a function of the delayed photon wavelength for nuclear recoil scintillation light emission spectrum at different recoil energies (delayed photon signal). **Right graph:** Photon kinematic spectrum probability distribution function as a function of the prompt photon wavelength for light emission in inverse Primakoff processes $a + N \rightarrow \gamma + N$ (prompt photon signal).

Events and N_γ at different recoil energies			
E_r [keV]	0.4	0.8	1.2
Events/min	325	95	32
N_γ /min	389	215	106

TABLE I: Number of events and photons generated in nuclear recoils at different recoil energies for $\Delta t = 1$ min and for the parameter space point $m_a = 0.3$ MeV and $g_{a\gamma\gamma} = 9.5 \times 10^{-5} \text{ GeV}^{-1}$. These values are used to generate the scintillation light spectra shown in Fig. 5.

As we have already anticipated, the fact that the scattering process itself produces final-state photons might enable their identification (at least partially). In contrast to scintillation light produced in nuclear recoils—that requires a certain time to build up—these photons are produced directly in the scattering process. This implies a time delay that could be used to separate signal from background, in the same way it is done in electron anti-neutrino detection. In other words, here we want to argue that final-state photons produce a prompt photon component while nuclear recoils a delayed one.

The identification of the prompt signal requires at least the characterization of the photon kinematic spectrum PDF. This can be done by noting that final-state photons within a narrow energy range produce nuclear recoils with fixed recoil energy. Since $E_a \simeq E_\gamma$, that range can be determined with the aid of Eq. (37)

$$E_\gamma = \sqrt{\frac{m_N E_r}{1 - \cos\theta}} \subset \sqrt{\frac{m_N E_r}{2}} \left[\frac{1}{\sin(\theta_{\max}/2)}, \frac{1}{\sin(\theta_{\min}/2)} \right]. \quad (42)$$

Here θ_{\min} is fixed by the kinematic constraint $E_\gamma^{\max} = 10$ MeV. So, given a certain recoil energy one finds

$$\theta_{\min} = 2 \arcsin \left(\frac{1}{E_\gamma^{\max}} \sqrt{\frac{m_N E_r}{2}} \right). \quad (43)$$

To determine θ_{\max} we adopt $\theta_{\max} = \theta_{\min} + \Delta\theta$, with $\Delta\theta = \pi/18$. This choice is motivated by the observation that Primakoff scattering produces mostly forward photons. With the photon energy range fixed, and for the recoil energy values and corresponding events in Tab. I, we have randomly sampled E_γ .

Results for the prompt photon kinematic spectrum PDF are shown in Fig. 5 (right graph). In contrast to the scintillation light emission PDF, whose profile follows the Gaussian emission profile, in this case the spectra are rather flat, narrow, and in the X-ray part of the electromagnetic spectrum. Note that since the JUNO-TAO cocktail involves a wavelength shifter (BisMSB), these wavelengths might shift towards larger values.

Having characterized the prompt photon kinematic spectrum PDF, we are now in a position to quantify the time delay between the two signals. In general, photons produced in nuclear (or electron) recoils and/or final-state photons produced in the ALP-nucleus (or electron) interactions have a non-zero likelihood of being reprocessed by the medium (LAB). There is also a non-zero probability that some of those photons reach a SiPM with no further interaction. These fractions can be estimated with the aid of a simplified version of production and detection, as we now discuss.

To do so, we have randomly sampled over a two-dimensional projection of the JUNO-TAO fiducial volume. This allows the generation of production points. We then randomly sample detection points over the active volume boundary. Production and detection points determine the photon trajectory lengths, which can then be compared with the photon mean free path of the compound (assumed to be $\text{C}_6\text{H}_5\text{C}_{13}\text{H}_{27}$, for definiteness), extracted from Ref. [61]. A schematic sample of the output is shown in Fig. 6.

Randomly assigning energies to those events, the survival

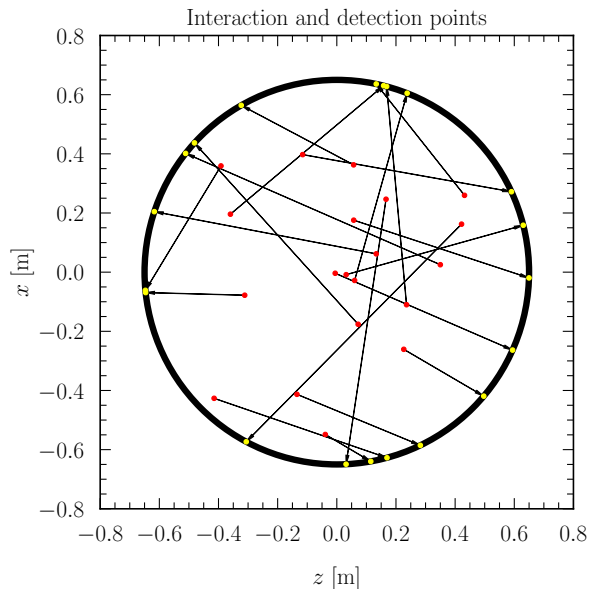


FIG. 6: Schematic sample of final-state photons production points (red) and detection points (yellow). This graph illustrates the procedure we have employed in the determination of the survival probability for a given fraction of photons.

probability for photon propagation can be written as

$$\mathcal{P}(E_\gamma) = e^{-d(E_\gamma)/\ell(E_\gamma)}, \quad (44)$$

where $d(E_\gamma)$ stands for the length of each photon trajectory and $\ell(E_\gamma)$ to the photon mean free path in $\text{C}_6\text{H}_5\text{C}_{13}\text{H}_{27}$. Sampling over Eq. (44)—after constructing the sample $d(E_\gamma)$ —allows the determination of the fraction of photons that have a certain probability of reaching a SiPM without further interacting with the target material. Results are displayed in Fig. 7. The left graph shows the photon mean free path, while the right graph shows the fraction of photons in terms of their survival probability. From the latter, one can see that about 5% of those photons have a 40%-50% probability of reaching a SiPM without further interacting with the medium.

There is, of course, the question of what are the most probable photon energies for which that will be the case. Given the expression for the survival probability—Eq. (44)—and the photon mean free path, it is clear that the most likely photons to get from production to detection without interacting with the medium are close to the high energy tail. Those photons are produced by the most energetic ALPs, which in turn are less abundant. So, despite having a relatively large fraction, they are expected to be less abundant just because of kinematic criteria.

A photon produced in an interaction taking place in a random point $d \in [0, 0.65]$ m within the active volume will reach a SiPM in a time given by $t_{\text{int}} = d/v_\gamma$, with $v_\gamma = c/n_{\text{LAB}}$ and n_{LAB} the refractive index for LAB [76]. A recoiling nucleus—instead—will transfer energy to the medium during τ_{recoil} , after which the medium will undergo de-excitation during τ_{decay} . The scintillation photons produced in these processes

will then reach the SiPM after t_{int} . One can then write

$$\begin{aligned} t_{\text{prompt}} &= t_{\text{int}}, \\ t_{\text{delayed}} &= \tau_{\text{recoil}} + \tau_{\text{decay}} + t_{\text{int}}. \end{aligned} \quad (45)$$

The time elapsed between the prompt and the delayed signals can then be estimated to be $\tau = t_{\text{delayed}} - t_{\text{prompt}} = \tau_{\text{recoil}} + \tau_{\text{decay}}$. Here we have assumed that the photons are not reprocessed by the medium (a small fraction will, as we have previously demonstrated). Assuming otherwise will add an additional term (t_{repro}) common to both signals, that will cancel in τ .

For the calculation of t_{delayed} we have assumed $\tau_{\text{recoil}} \ll \tau_{\text{decay}}$, with $\tau_{\text{recoil}} \in [0, 1]$ ns. For τ_{decay} we assume a Gaussian distribution with mean located at $\bar{\tau}_{\text{decay}} = 4.69$ ns and standard deviation $\sigma = 1.5$ ns [77]. Results are shown in Fig. 8, where it can be seen that the average time window amounts to about 5 ns.

All in all, it seems to us that ALP signals through Primakoff processes might be identifiable by using the delay between the two types of light signals they involve. For this to be the case, the SiPM array should be able to separate signals within a ~ 5 ns window³. Furthermore, the light yield in nuclear recoils should be intense enough. If these two requirements are met, identification appears to be feasible (at least in certain regions of parameter space).

ALP decay through $g_{\alpha\gamma\gamma}$ produces no nuclear recoil. In the ALP decay-rest-frame (RF), two back-to-back photons with $E_{\gamma_1}^* = E_{\gamma_2}^* = E_\gamma^* = m_a/2$ are produced (γ_1 and γ_2 refer to the final-state photons and E_γ^* to energy measured in the RF). The signal, however, is observed in the laboratory frame (LF). Thus, in order to determine their spectrum we assume—in full generality—that in the RF

$$\vec{p}_1 = m_a(\sin\theta^* \sin\varphi^*, \sin\theta^* \cos\varphi^*, \cos\theta^*)/2, \quad (46)$$

with $\vec{p}_1 = -\vec{p}_2$ (as dictated by momentum conservation). For an ALP propagating along a unitary vector $\hat{n} = (\sin\theta \sin\varphi, \sin\theta \cos\varphi, \cos\theta)$ in the laboratory frame (LF), a general Lorentz transformation enables writing

$$\begin{aligned} E_{\gamma_1} &= \frac{m_a}{2} \gamma \left[1 + \vec{\beta} \cdot \hat{n} \right], \\ E_{\gamma_2} &= \frac{m_a}{2} \gamma \left[1 - \vec{\beta} \cdot \hat{n} \right], \end{aligned} \quad (47)$$

with the boost and velocity factors given by $\gamma = E_a/m_a$ and $|\vec{\beta}| = \sqrt{\gamma^2 - 1}/\gamma$. Note that Eq. (47) is inline with expectations: $E_{\gamma_1} + E_{\gamma_2} = m_a\gamma/2$. And that $E_{\gamma_i} \in \gamma m_a \left[1 - |\vec{\beta}|, 1 + |\vec{\beta}| \right] / 2$, subject to energy conservation.

³ As far as we understand, this time window will be unlikely to be reached with the current JUNO-TAO configuration. In contrast, with the more sophisticated CLOUD detector, such a discrimination may be obtained. Still, we believe interesting to develop here a first hypothetical computation for our generic detector and perform a specific study of this topic in future work.

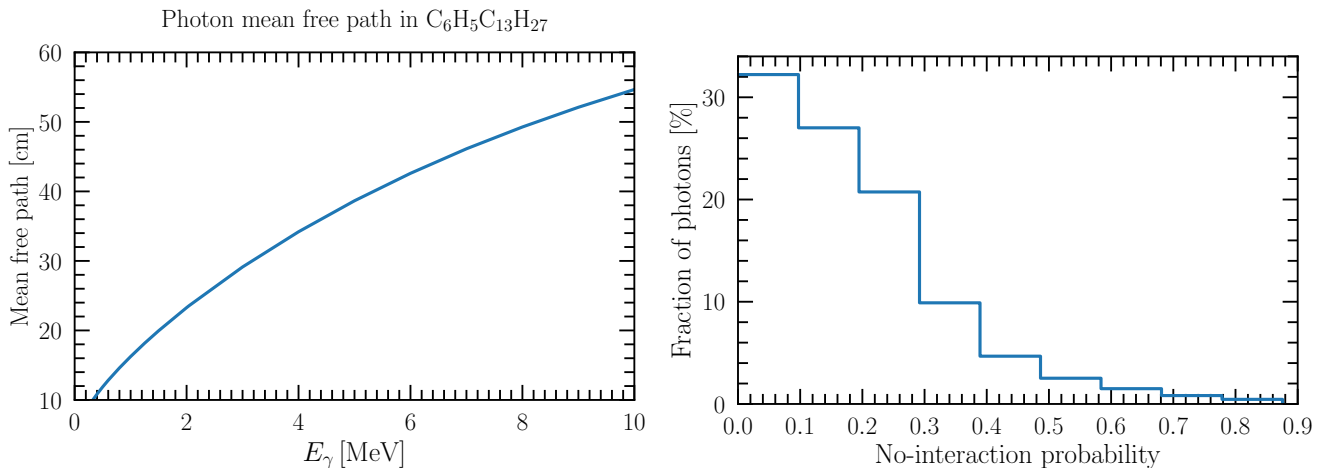


FIG. 7: **Left graph:** Photon mean free path in $C_6H_5C_{13}H_{27}$ as a function of photon energy [61]. **Right graph:** Fraction of photons that reach a SiPM without further interacting with the medium. From this result one can see that $\sim 5\%$ of those photons have a survival probability in the range 40% – 50%.

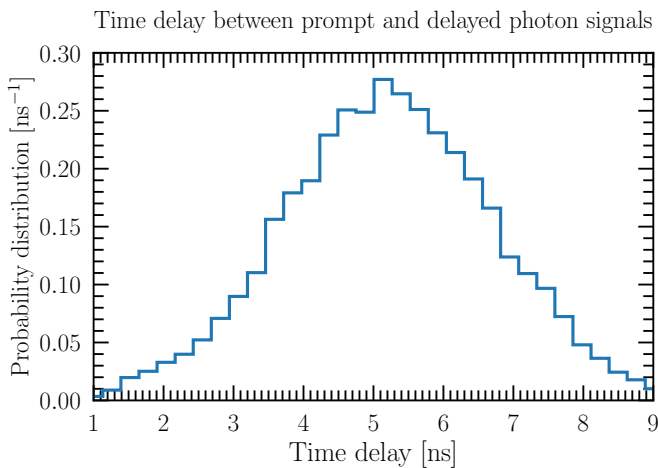


FIG. 8: Time delay for final-state photon signals and scintillation photons produced in nuclear recoil processes. Our main assumption here is that final-state photons reach the SiPM array after the interaction, with no reprocessing by the LAB cocktail (see text for details).

To determine the degree at which the photons are still back-to-back in the LF, one could rely on the photons 3-momentum components written in the LF. These expressions, however, are a complicated function of the angular variables. So we instead restore to 4-momentum conservation in the LF, from which it follows that

$$\cos \theta_{\gamma_1 \gamma_2} = 1 - \frac{m_a^2}{2E_{\gamma_1} E_{\gamma_2}}. \quad (48)$$

Eq. (48), along with those in Eq. (47), enable the determination of the photons relative direction PDF as well as the photons kinematic spectrum PDFs. To illustrate their behavior, we have sampled over 10000 events, assuming $E_a = 5 \text{ MeV}$ and $m_a = 1 \text{ MeV}$. Results are shown in Fig. 9.

In contrast to what happens in the RF, almost all events final-state photons are rather collinear⁴. Since in the laboratory frame $\vec{p}_a = \vec{p}_{\gamma_1} + \vec{p}_{\gamma_2}$, with $\vec{p}_a \neq \vec{0}$, this is somewhat expected. The kinematic spectrum distributions reveal another interesting feature. Although not very pronounced, events tend to cluster at the extremes of the allowed energy window. Thus, for those γ_1 clustering in the upper part of the interval, the same amount of γ_2 will cluster in the lower part of that range (and vice versa). So, ALP decays will produce two almost collinear photons, one carrying most of the available energy ($m_a \times \gamma$) and the other one only a small fraction. There are of course other configurations in which the available energy is more uniformly distributed, but according to the kinematic spectrum PDFs those events are less likely (although not drastically).

2. Inverse Compton-like scattering, axio-electric absorption and ALP decay to electron pairs

We now turn to the case of ALP-electron (*inverse Compton-like*) scattering. In many aspects, signals resemble those found in the inverse Primakoff case but with an enhancement in recoil energies, which favors signatures identification. The final-state photon energy follows from Eq.(36) by trading $m_N \rightarrow m_e$. Because of $E_a > m_e$, the process can produce either forward (E_{γ}^{\max}) or backward photons (E_{γ}^{\min}), in stark contrast to Primakoff scattering. Therefore, for forward (backward) photons, the final-state electron energy will reach a minimum (maximum), $E_{e_{\min, \max}} = E_a - E_{\gamma}^{\max, \min} + m_e$. Fig. 10 (left

⁴ This is just a manifestation of the relativistic beaming effect, whereof radiation emitted by a relativistic source is enclosed within a cone of half-angle $1/\gamma$. The more boosted the particle is, the more collinear the emitted photons will be.

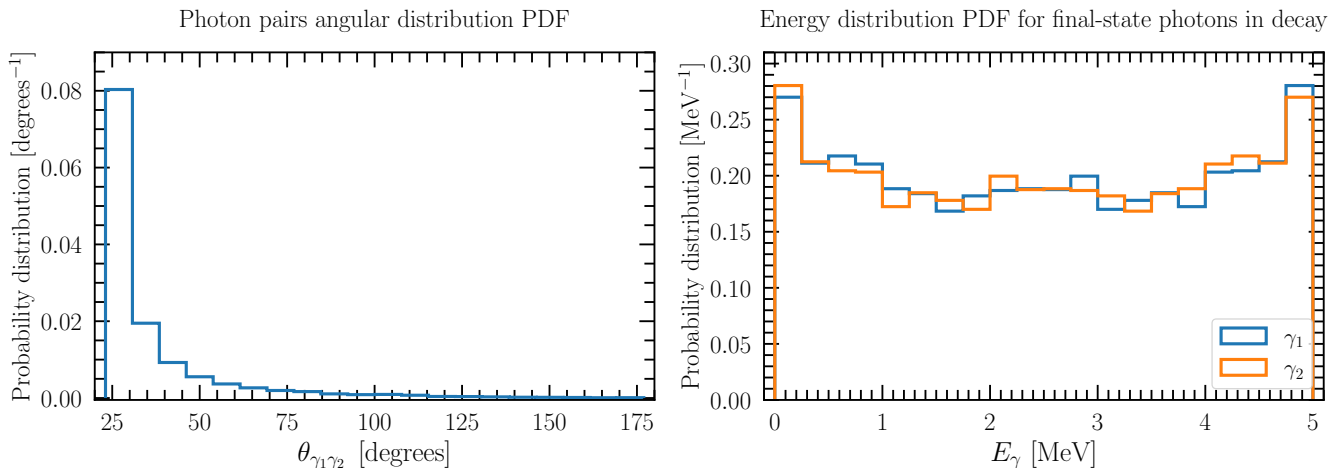


FIG. 9: **Left graph:** PDF for the relative direction between final-state photons produced in ALP decays and measured in the laboratory frame. **Right graph:** Final-state photons energy distribution PDF. For both calculations the kinematic point $E_a = 5$ MeV and $m_a = 1$ MeV has been chosen.

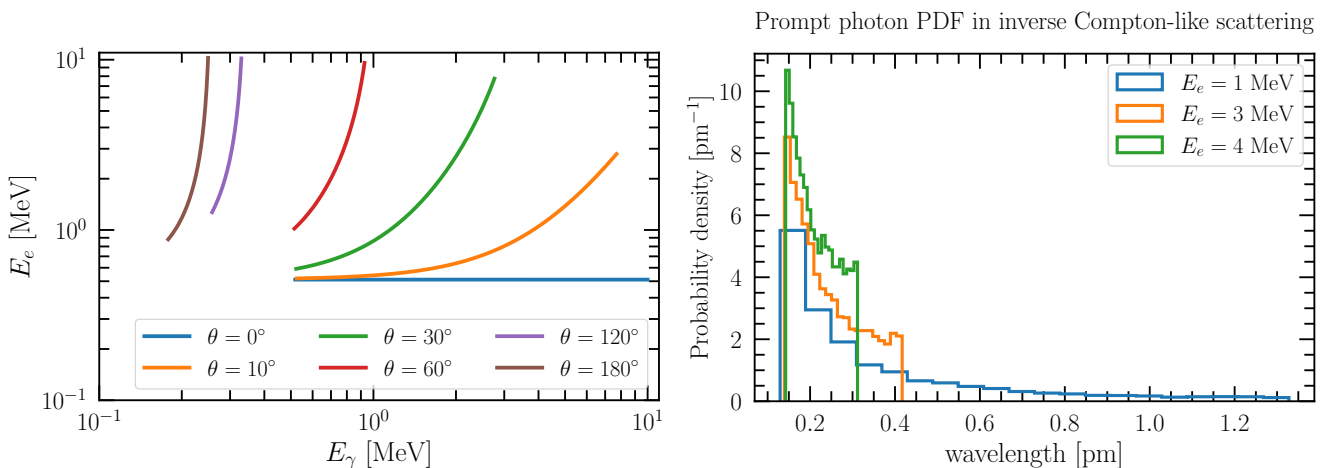


FIG. 10: **Left graph:** Final-state photon and electron energies in inverse Compton-like scattering calculated for $m_a = 100$ keV and different ALP and photon directions (θ). **Right graph:** Prompt photon kinematic spectrum (final-state photon) in inverse Compton-like scattering, assuming forward final-state electron (backward photon). The same ALP mass as in the left graph has been assumed.

graph) shows the behavior in terms of the direction of the incoming ALP and outgoing photon. Typical energies are of the order of MeV, but large photon energy values imply lower electron energies and vice versa.

Scintillation light from electron recoils produces then much more PEs than those produced in nuclear recoils. It can readily produce 4500 PEs, or even more depending on the relative direction between the ALP and the photon. The shape of the scintillation light spectrum (delayed signal) follows the Gaussian distribution in Fig. 4, and so the PDF for electron recoil scintillation light emission is expected to follow that in Fig. 5 (left graph).

For the prompt photon kinematic spectrum PDF, we have relied on momentum conservation which relates the initial-state ALP energy with that of the final-state electron and photon in terms of the ALP and electron direction (α). An exam-

ple of the PDF is shown in Fig. 10 (right graph), assuming forward electron events (backward photons). This result is, of course, representative of only that kinematic configuration and different values for α will produce different spectra. However, it shows that a full characterization of the prompt signal might be possible.

The time delay between the scintillation light produced in electron recoils and the final-state photons is not expected to change compared with that found in the Primakoff case. The conditions under which it was derived do not seem to depend on the recoiling particle. Thus, the combination of prompt and delayed signals—along with a larger number of PEs—indicate that detection of ALPs coupled to electrons is much more favorable than detection of ALPs coupled to light.

Axio-electric absorption will happen mainly on carbon atoms, as it is the case for inverse Primakoff and Compton-like

scattering. Carbon atomic electron configuration is $1s^2 2s^2 2p^2$: K-shell, (full filled $1s$ subshell) and L-shell (full filled $2s$ subshell and partially filled $2p$ subshell). In the process, an ALP gets absorbed, and an electron is ejected. Its kinetic energy is given by

$$T_e = E_a - B, \quad (49)$$

where B is the binding energy of the ejected electron. Given the average energy of the initial-state ALPs, ejected electrons will come from the K-shell. For a free carbon atom, the K-shell binding energy is ~ 284.3 eV [78], which means that $T_e \simeq E_a$. After ejection, an L-shell electron will fill the K-shell vacancy. In carbon—and in general, in low Z atoms—the likelihood for photon emission is low, so atomic reconfiguration produces an Auger electron instead [79]: The L-shell to K-shell transition will transfer energy to another L-shell electron that will be ejected. The energy of the Auger electron can then be written as

$$E_{\text{Auger}} = E_K - E_{L_1} - E_{L_2}, \quad (50)$$

where E_K is the K-shell binding energy and E_{L_1} and E_{L_2} are the binding energies for $2s$ and $2p$ electrons, respectively. Their values—taken from Ref. [78]—are $E_{L_1} \simeq 18.10$ eV and $E_{L_2} \simeq 11.30$ eV, so $E_{\text{Auger}} = 254.9$ eV. All in all, axio-electric absorption produces first an electron with energy $E_e = m_e + T_e \approx m_e + E_a$, followed by an Auger electron with a well determined energy.

Thus, in this case as well, one can properly define a prompt and a delayed signal with a time window determined by the time elapsed between axio-electron emission and Auger emission. Experimental studies of those time windows for neon, using intense X-ray free-electron lasers, have shown $\tau_{\text{Auger}} = 2.2$ fs [80]. The order of magnitude for the time window in this case is, therefore, 1 fs. There are, of course, some caveats to this discussion, of which we would like to mention at least two. First of all, Auger electrons are very soft electrons and so once emitted they might be absorbed by the medium. If this is the case, they will not leave a measurable signature. Secondly, for the prompt and delayed signals to be of any use, the SiPMs should have time resolutions in the fs range. For that reason, we only want to stress that if the conditions we have outlined could somewhat be met, the possible background that axio-electric absorption might face could perhaps be largely mitigated.

We now turn to the final process that ALP-electron couplings enable, namely, *ALP decay to e^+e^- pairs*. Differences with decay to final-state photons arise only because of the massive final states. The electron and positron energies are dictated by expressions like those in Eq. (47), with the last term traded according to $\vec{\beta} \cdot \hat{n} \rightarrow \vec{\beta} \cdot \vec{v}_e$ ($|\vec{v}_e| = \sqrt{1 - 4m_e^2/m_a^2}$ the electron/positron velocity). The electron and positron energies are then in the MeV range. Accordingly, their propagation in the detector medium will produce an abundant amount of scintillation light. In the LAB frame, their relative direction $\theta_{e^-e^+}$ is given by

$$\cos \theta_{e^-e^+} \simeq 1 - \frac{m_a^2 - 2m_e^2}{2E_{e^+}E_{e^-}}, \quad (51)$$

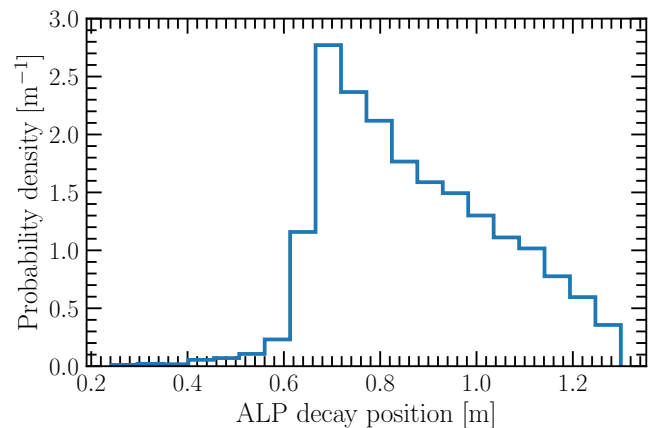


FIG. 11: ALP decay position (within the fiducial volume) probability density function as a function of decay position. The most likely point is found at $r = 0.7$ m. For ALP decay event rates, we fix the detector depth to that value.

where we have used the fact that—in general—the electron-positron pair is very boosted and so $|p_{e^\pm}| \gg m_e$. Compared with Eq. (48), one would expect the opening angle to be smaller than in the final-state photon case. This, however, is not the case because of the kinematic constraint $m_a > 2m_e$. So, regions where the electron mass could produce a sizable suppression of the second term in Eq. (51) are not kinematically accessible. Thus, pairs produced in ALP decays are expected to be as well rather collinear. A fraction—likely small—will reach the SiPMs, and the others will produce an abundant amount of photons (scintillation light). Electrons will generate scintillation light, and positrons—instead—will annihilate with electrons, producing in doing so a broad spectrum around the 511 keV line.

IV. SENSITIVITIES

In this section, we discuss ALP search sensitivities at the JUNO-TAO detector. For that aim, we rely on the results presented in Secs. II and III. In particular, we entertain the possibility that because of the prompt and delayed photon signals, as well as the distinctive imprints left by the ALP decay by-products, searches may be potentially background-free.

ALP event rates in LAB are mainly determined by carbon nuclei, as can be seen from the hydrogen and carbon mass fractions

$$f_C^n = \frac{m_C(n+6)}{m_{\text{LAB}}}, \quad f_H^n = \frac{m_H(2n+6)}{m_{\text{LAB}}}. \quad (52)$$

Here, we assume $\text{C}_6\text{H}_5\text{C}_{13}\text{H}_{27}$ as a material target while neglecting all the other components of the JUNO-TAO cocktail. An assumption well justified given their relative small amounts. For this compound, we find that carbon contributes to 88% of the total mass. Relevant for the event rate calculation as well are the nuclear reactor power, the baseline, and detector radius, which we fix to $P = 4.6$ GW, $L = 30$ m, and $R_{\text{JUNO-TAO}} = 0.65$ m (active volume radius).

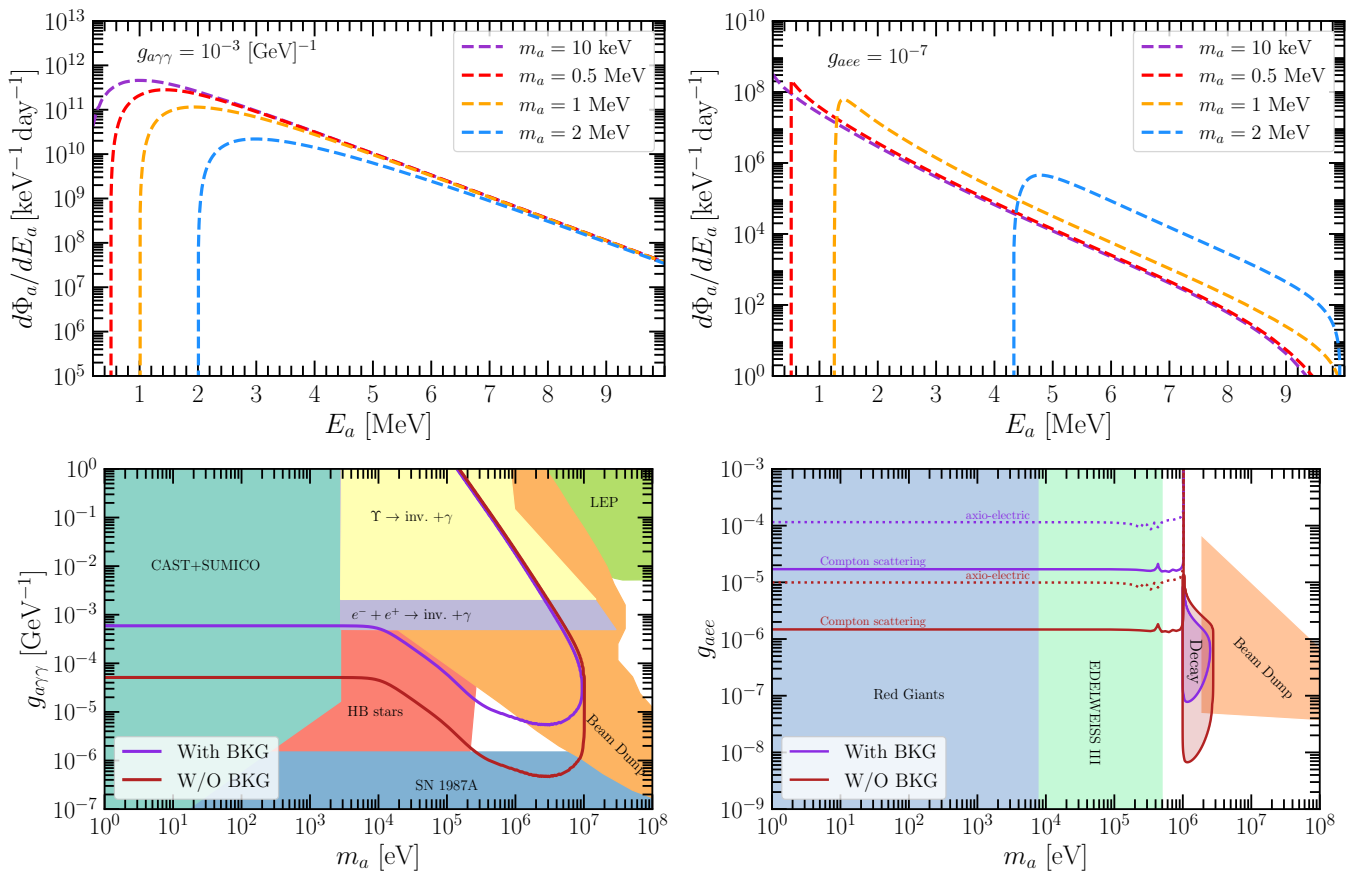


FIG. 12: **Upper left graph:** Expected ALP fluxes from Primakoff scattering processes as a function of ALP energies for different ALP masses and $g_{a\gamma\gamma} = 10^{-3} \text{GeV}^{-1}$. **Upper right graph:** Same as upper left graph but for Compton-like scattering processes. **Lower left graph:** 90% CL sensitivities, obtained by assuming an exposure of 180 days, shown in the $g_{a\gamma\gamma} - m_a$ plane for two extreme scenarios: (i) Full background (from singles from radioactivity [53]) plus signal, (ii) background-free searches. **Lower right graph:** Same as lower left graph, but in the $g_{aee} - m_a$ plane.

For event rates from ALP decays, the detector depth, r , is also required [see Eq. (10)]. Given the geometry, we proceed by noting that the detector will be deployed at the Taishan Neutrino Laboratory located in a basement at 9.6 m underground [53]. With that information, along with the detector fiducial volume radius and baseline, a simple two-dimensional model of ALP decay within the fiducial volume can be constructed (see App. A). That model enables the determination of the most likely point at which decay will happen. Fig. 11 shows the probability distribution function in terms of the decay point length. This result shows that decays happen more often at $r \in [0.66, 0.72] \text{m}$, and so we fix $r = 0.7 \text{m}$ in our calculation.

The expected qualitative behavior of sensitivities can be understood already from the results presented in Sec. II. Fig. 12 (upper panels) shows results for the predicted ALP fluxes in terms of ALP energies. First of all, since at low ALP masses the differential cross sections have little dependence upon m_a , ALP fluxes are degenerate regardless of the production mechanism. At high ALP energies, close to threshold, fluxes tend to degenerate as well. An effect attributed to the fact that as energy increases terms that involve ALP masses become sub-

dominant.

For the Primakoff and inverse Primakoff case, this implies that for $m_a \lesssim 10 \text{keV}$ sensitivities depend only on $g_{a\gamma\gamma}$. For masses up to 100keV , terms involving ALP masses in the scattering cross-section are still of little relevance. However, at those masses, the decay width reaches values such that the decay probability becomes sizable enough [the decay width scales as m_a^3 , see Eq. (4)]. Thus, event rates will become sensitive to ALP masses with increasing ALP mass. Scattering processes will also introduce a mass dependence, which will be mild due to the decreasing fluxes. The strongest dependence on ALP mass is thus expected from ALP decays.

For processes controlled by the g_{aee} coupling, sensitivities are expected to be ALP mass independent up to larger ALP masses. In the low-mass region fluxes are rather degenerate. With increasing ALP mass, that degeneracy is to a certain extent lifted, but with decreasing fluxes (see Fig. 12, right upper graph). Thus, as in the case of the $g_{a\gamma\gamma}$ coupling, the most pronounced ALP dependence is introduced by decays. In this case—however—the decay becomes effective only when $m_a > 1 \text{MeV}$ value at which there is no flux for a large enough coupling. For an ALP to reach the detector, its decay length

should exceed the reactor-detector baseline, implying the constraint

$$g_{aee} \lesssim \frac{8\pi \hbar c}{L m_a \sqrt{1 - 4m_e^2/m_a^2}}. \quad (53)$$

This limit is satisfied for any ALP mass in the kinematically allowed range provided $g_{aee} \lesssim 10^{-7}$.

With the qualitative behavior discussed, we then determine sensitivities with the aid of the following χ^2 function

$$\chi^2(g_X, m_a) = \frac{N_{\text{signal}}^2(g_X, m_a)}{N_{\text{signal}}(g_X, m_a) + N_{\text{bckg}} + N_{\text{signal}}^2 \sigma_{\text{sig}}^2}. \quad (54)$$

Here N_{signal} is the number of ALP events for a point in parameter space $\{g_X, m_a\}$ ($g_X = g_{\alpha\gamma\gamma}$ or $g_X = g_{aee}$), N_{bckg} is the number of background events, and σ_{sig}^2 the signal systematic uncertainty. Note that when writing the χ^2 function as in Eq. (54) we are assuming that the background systematic uncertainty, σ_{bckg} , amounts to zero. This is certainly not the case, but we have checked that the signal systematic uncertainty has little impact and so found no reason for the background systematic uncertainty to do so. We have fixed $\sigma_{\text{sig}} = 0.1$.

Results for 90% CL sensitivities (obtained by the condition $\chi^2(g_X, m_a) = 4.61$ for 2 degrees of freedom) are shown in the lower graphs of Fig. 12. Lower left panel in the $g_{\alpha\gamma\gamma} - m_a$ plane, while the lower right panel in the $g_{aee} - m_a$ plane. Results are presented for two extreme search scenarios: (i) Signal+background and (ii) signal alone (background-free). At JUNO-TAO, ALP searches are subject to an abundant background, which includes: IBD, fast neutrons after veto, and singles from radioactivity (see e.g. Refs. [53, 75] for details). Particularly threatening are the latter, which are overwhelmingly larger than those from IBD or fast neutrons, amounting to about 10^9 events/year.

Sensitivities in the signal+background scenario—calculated for a six-month data-taken period—thus include only the singles from radioactivity background, in line with the analysis presented in Ref. [54]. The background-free scenario is motivated by results from Sec. III which show: Presence of prompt and delayed photon signals in scattering processes, coincident events in the case of ALP decays, and prompt (scintillation light) and delayed signals (Auger electrons) from axio-electric absorption. When presenting results for this scenario, we do not aim at suggesting that such an ideal case can be experimentally achieved. Instead our idea is that of showing that actual results might—in principle—interpolate between the worst-case (signal+background) and best-case (background-free) scenarios.

In the case of the nuclear channel, sensitivities in scenario (i) indicate that a certain portion of the cosmological triangle can be explored. This region is subject to constraints from Big Bang nucleosynthesis and from the effective number of relativistic species [23–25]. In terms of the Λ CDM model, where inflation is assumed to have happened at very early times, it is therefore ruled out. It opens up, however, in e.g. low-reheating models [25]. Testing this region in a controlled experimental environment, therefore, provides an indirect test for nonstandard cosmological scenarios. Reducing

the background will improve this result up to the point where the whole cosmological triangle can be thoroughly covered, provided background-free searches can be carried out with the aid of the prompt and delayed photon signals we have identified. It will enable as well to enter the region where horizontal branch (HB) stars and supernova (SN) constraints apply. Thus, it will test ALP models where medium effects forbid their production in astrophysical environments (see e.g. Ref. [32]).

Results in Fig. 12 (lower left graph) include as well 90% CL constraints from other astrophysical and laboratory experiments. CAST and SUMICO solar axion searches [81, 82], HB stars, and SN1987A [20–22]. The latter derived from stellar cooling and SN energy loss arguments. Laboratory searches include rare Υ invisible decays, exotic final states in e^+e^- collisions (including LEP) and beam dump searches [26–31]

Turning to the case of the electron channel, sensitivities can highly improve in the background-free case as well. Results in the signal+background scenario show that in regions of MeV ALP masses, sensitivities go down to couplings of the order of 10^{-7} . Background-free searches will be able to scan couplings more than one order of magnitude smaller. Interestingly, as far as we know, this region is unexplored. So, if the background can be efficiently mitigated this region might be thoroughly explored. Taking advantage of coincident events from ALP decays, discussed in Sec. III, might help in doing so. Furthermore, models where environmental effects are at work can be tested in those regions where Red Giants constraints apply [19]. Note that further limits, in this case, include searches in the EDELWEISS-III array of germanium bolometers [83] and beam dump laboratory searches [84].

V. CONCLUSIONS

In this paper, we have studied the capability of a JUNO-TAO-like detector concept as a case study of ALP searches in short-baseline neutrino experiments using large organic liquid scintillator detectors. To do so, we have considered ALP couplings to photons and electrons. In the former case, our analysis includes production through Primakoff-like scattering processes and detection through its inverse equivalent and decay to photon pairs. In the latter, instead, production induced by Compton-like scattering processes and detection through all the possible channels the coupling allows for (apart from e^+e^- pair production in the electron field): Inverse equivalent process, axio-electric absorption, and decay to e^+e^- pairs.

We have shown that signals in both nuclear and electron recoil processes produce prompt and delayed photon signals. The prompt component arises from the final-state photon produced in the scattering process itself. The delayed signal, instead, from scintillation light produced by the recoil. The time window, estimated to be of the order of 5 ns (for the experimental parameter configuration considered), has its origin in the time it takes the scintillation light to be built. We have pointed out that if the SiPMs can resolve this time window, an efficient radioactive background rejection might be possible. Although we have considered a generic liquid scintillator

detector, when comparing with detectors currently under construction, we find that the CLOUD experiment may be more adequate for exploring this time window and deserves a more dedicated study. In such scenario, we have demonstrated that sensitivities can improve largely. If this turns out to be the case, a full exploration of the so-called cosmological triangle seems feasible. Furthermore, in the case of ALPs coupled to electrons it will improve sensitivities by one order of magnitude allowing for searches in regions not yet explored.

In the case of axio-electric absorption, we have found as well a prompt and a delayed component. Ejected electrons from carbon atoms K-shells will be followed by Auger electrons in a very narrow time window of the order of 1 fs. We have argued that time resolution, along with the small amount of scintillation light produced by the Auger electron, seems to be an experimental challenge. If these two issues can be properly addressed, background effects may be efficiently mitigated.

Decays will directly produce photon pairs in the case of ALPs coupled to photons. They will produce scintillation light and a broaden spectrum around 511 keV from e^+e^- annihilation, in the case of ALPs coupled to electrons. In both cases, the signals will be subject to relativistic beaming effects and so will lead to coincident photon events with small opening angle. Assuming small diffusion effects, this will translate into activation of nearby SiPMs.

All in all, by using a JUNO-TAO-like detector concept we have argued that short-baseline large liquid scintillator detectors are very well suited for ALP searches in the MeV mass window. Both electron and nuclear scattering seem to be promising channels, in particular, if the experimental challenges we have identified can be overcome. If so, it seems to us that this technology can provide valuable information on the global ALP search program.

Acknowledgments

We would like to thank Anatael Cabrera and Dimitrios Papoulias for useful discussions and comments on this paper. D.A.S. is supported by ANID grant ‘‘Fondecyt Regular’’ 1221445, and H.N. by CNPq and CAPES from Brazil. O.G.M. would like to thank support from Sistema nacional de investigadoras e investigadores (SNI) from Mexico. Two of us (D.A.S. and H.N.) thank CINEVESTAV for the hospitality during the initial stage of this work.

Appendix A: Fiducial volume ALP decay

Here we present the details of the two-dimensional model adopted for the determination of the ALP most likely decay point. Relying on the sketch in Fig. 13, one can write

$$|\Delta\vec{r}|^2 = |\vec{r}_{\text{det}}|^2 + |\vec{r}_a|^2 - 2|\vec{r}_{\text{det}}||\vec{r}_a|\cos\theta_a, \quad (\text{A1})$$

where θ_a is the angle between the fixed vector \vec{r}_{det} and the ALP position vector measured from the production point (assuming a point-like source) to the interaction point. Its norm is given by $|\vec{r}_{\text{det}}|^2 = (b+R)^2 + (d+R)^2$, where $R = 0.65$ m is the detector fiducial volume radius. For the interaction to take place within the fiducial volume, the condition $|\Delta\vec{r}| \leq [0, R]$ must be satisfied. With that information at hand, Eq. (A1) can be solved for $|\vec{r}_a|$ resulting in

$$|\vec{r}_a|_{\pm} = |\vec{r}_{\text{det}}|\cos\theta_a \pm \sqrt{|\Delta\vec{r}|^2 - \sin^2\theta_a|\vec{r}_{\text{det}}|^2}. \quad (\text{A2})$$

For this equation to be meaningful the following constraint must be satisfied

$$-\frac{|\Delta\vec{r}|}{|\vec{r}_{\text{det}}|} \leq \sin\theta_a \leq \frac{|\Delta\vec{r}|}{|\vec{r}_{\text{det}}|}. \quad (\text{A3})$$

ALPs that satisfy this condition will pass by the detector. With this condition, one can then run a simple, yet useful, Monte Carlo as follows. Randomly sample $|\Delta\vec{r}|$ in the interval $[0, R]$ N times. For each point, calculate randomly $\sin\theta_a$ in the interval dictated by condition (A3). The random values $|\Delta\vec{r}|$ and θ_a obtained in this procedure allow then to determine an interval for $|\vec{r}_a|$: $[|\vec{r}_a|_-, |\vec{r}_a|_+]$. From this interval, a random value for $|\vec{r}_a|$ can be selected for each of the N events generated.

The information from the Monte Carlo can then be used to determine the detector ‘‘depth’’ (point where the interaction takes place, decay in this case), namely (see inset sketch in Fig. 13)

$$r = L_{\text{AE}} + L_{\text{EB}}. \quad (\text{A4})$$

First of all, from the triangle defined by vertices PBC one finds $\beta = \pi/2 - \theta_a$. From the triangle defined by vertices BCD, instead,

$$\cos\rho = \frac{L_{\text{BC}}}{|\Delta\vec{r}|} = \frac{|\vec{r}_a \sin\theta_a|}{|\Delta\vec{r}|}. \quad (\text{A5})$$

Since $\alpha = \beta - \rho$, Eq. (A5) along with the value for β thus allows writing from the triangle defined by vertices DEB

$$L_{\text{EB}} = |\Delta\vec{r}|\cos\alpha. \quad (\text{A6})$$

From the same triangle, one can as well write $L_{\text{ED}} = |\Delta\vec{r}|\sin\alpha$, which then, from the triangle defined by vertices DEA, one finds

$$L_{\text{AE}} = \sqrt{R^2 - L_{\text{ED}}^2}. \quad (\text{A7})$$

Eqs. (A6) and (A7), along with Eq. (A4), define the detector depth in terms of randomly generated quantities and so enable the construction of the PDF shown in Fig. 11.

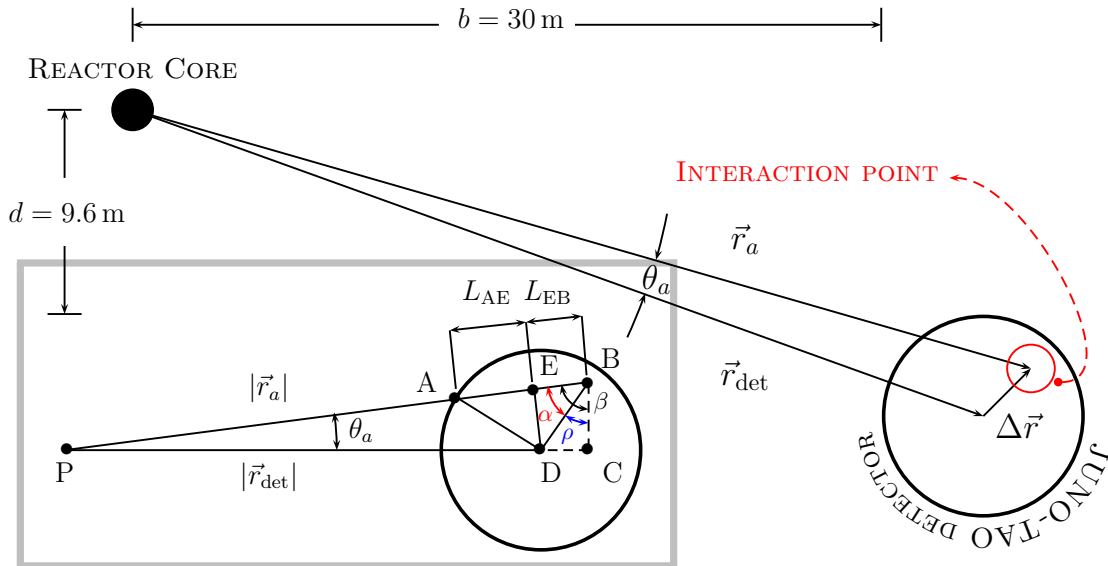


FIG. 13: Not-to-scale sketch of the two reactor cores of the Taishan Nuclear Power Plant and the JUNO-TAO detector. ALP trajectory is determined by \vec{r}_a , while the interaction point within the detector fiducial volume by $\Delta\vec{r} = \vec{r}_a - \vec{r}_{\text{det}}$. Baseline, $b = 30$ m, as well as detector depth, $d = 9.6$ m, are taken from Ref. [53]. This sketch is employed in the determination of the most likely ALP decay location. The inset sketch shows the geometry employed for the determination of the ALP most likely decay point within the fiducial volume.

- [1] R. D. Peccei and H. R. Quinn, “CP Conservation in the Presence of Instantons,” *Phys. Rev. Lett.* **38** (1977) 1440–1443.
- [2] S. Weinberg, “A New Light Boson?,” *Phys. Rev. Lett.* **40** (1978) 223–226.
- [3] F. Wilczek, “Problem of Strong P and T Invariance in the Presence of Instantons,” *Phys. Rev. Lett.* **40** (1978) 279–282.
- [4] Y. Chikashige, R. N. Mohapatra, and R. D. Peccei, “Are There Real Goldstone Bosons Associated with Broken Lepton Number?,” *Phys. Lett. B* **98** (1981) 265–268.
- [5] B. Batell, M. Pospelov, and A. Ritz, “Probing a Secluded $U(1)$ at B-factories,” *Phys. Rev. D* **79** (2009) 115008, arXiv:0903.0363 [hep-ph].
- [6] G. Grilli di Cortona, E. Hardy, J. Pardo Vega, and G. Villadoro, “The QCD axion, precisely,” *JHEP* **01** (2016) 034, arXiv:1511.02867 [hep-ph].
- [7] M. Srednicki, “Axion Couplings to Matter. 1. CP Conserving Parts,” *Nucl. Phys. B* **260** (1985) 689–700.
- [8] K. Ehret *et al.*, “New ALPS Results on Hidden-Sector Lightweights,” *Phys. Lett. B* **689** (2010) 149–155, arXiv:1004.1313 [hep-ex].
- [9] M. Betz, F. Caspers, M. Gasior, M. Thumm, and S. W. Rieger, “First results of the CERN Resonant Weakly Interacting sub-eV Particle Search (CROWS),” *Phys. Rev. D* **88** no. 7, (2013) 075014, arXiv:1310.8098 [physics.ins-det].
- [10] OSQAR Collaboration, R. Ballou *et al.*, “New exclusion limits on scalar and pseudoscalar axionlike particles from light shining through a wall,” *Phys. Rev. D* **92** no. 9, (2015) 092002, arXiv:1506.08082 [hep-ex].
- [11] G. Ruoso *et al.*, “Limits on light scalar and pseudoscalar particles from a photon regeneration experiment,” *Z. Phys. C* **56** (1992) 505–508.
- [12] R. Cameron *et al.*, “Search for nearly massless, weakly coupled particles by optical techniques,” *Phys. Rev. D* **47** (1993) 3707–3725.
- [13] D. J. Kapner, T. S. Cook, E. G. Adelberger, J. H. Gundlach, B. R. Heckel, C. D. Hoyle, and H. E. Swanson, “Tests of the gravitational inverse-square law below the dark-energy length scale,” *Phys. Rev. Lett.* **98** (2007) 021101, arXiv:hep-ph/0611184.
- [14] A. Zehnder, “Axion Search in a Monochromatic γ Transition: A New Lower Limit for the Axion Mass,” *Phys. Lett. B* **104** (1981) 494–498.
- [15] J. F. Cavaignac *et al.*, “A Search for Axions at a Power Reactor,” *Phys. Lett. B* **121** (1983) 193–197.
- [16] P. Lehmann, E. Lesquoy, A. Muller, and S. Zylberajch, “AXION SEARCH IN THE MONOCHROMATIC M1 TRANSITION OF CU-65,” *Phys. Lett. B* **115** (1982) 270–272.
- [17] F. T. Avignone, III, R. L. Brodzinski, S. Dimopoulos, G. D. Starkman, A. K. Drukier, D. N. Spergel, G. Gelmini, and B. W. Lynn, “Laboratory Limits on Solar Axions From an Ultralow Background Germanium Spectrometer,” *Phys. Rev. D* **35** (1987) 2752.
- [18] TEXONO Collaboration, H. M. Chang *et al.*, “Search of axions at the Kuo-Sheng nuclear power station with a high-purity germanium detector,” *Phys. Rev. D* **75** (2007) 052004, arXiv:hep-ex/0609001.
- [19] G. G. Raffelt, “Astrophysical axion bounds,” *Lect. Notes Phys.* **741** (2008) 51–71, arXiv:hep-ph/0611350.
- [20] G. Lucente, P. Carena, T. Fischer, M. Giannotti, and A. Mirizzi, “Heavy axion-like particles and core-collapse supernovae: constraints and impact on the explosion mechanism,” *JCAP* **12** (2020) 008, arXiv:2008.04918 [hep-ph].
- [21] P. Carena, O. Straniero, B. Döbrich, M. Giannotti, G. Lucente, and A. Mirizzi, “Constraints on the coupling with photons of heavy axion-like-particles from Globular Clusters,”

- Phys. Lett. B* **809** (2020) 135709, arXiv:2004.08399 [hep-ph].
- [22] A. Ayala, I. Domínguez, M. Giannotti, A. Mirizzi, and O. Straniero, “Revisiting the bound on axion-photon coupling from Globular Clusters,” *Phys. Rev. Lett.* **113** no. 19, (2014) 191302, arXiv:1406.6053 [astro-ph.SR].
- [23] M. Millea, L. Knox, and B. Fields, “New Bounds for Axions and Axion-Like Particles with keV-GeV Masses,” *Phys. Rev. D* **92** no. 2, (2015) 023010, arXiv:1501.04097 [astro-ph.CO].
- [24] D. Cadamuro and J. Redondo, “Cosmological bounds on pseudo Nambu-Goldstone bosons,” *JCAP* **02** (2012) 032, arXiv:1110.2895 [hep-ph].
- [25] P. F. Depta, M. Hufnagel, and K. Schmidt-Hoberg, “Robust cosmological constraints on axion-like particles,” *JCAP* **05** (2020) 009, arXiv:2002.08370 [hep-ph].
- [26] **Crystal Ball** Collaboration, D. Antreasyan *et al.*, “Limits on axion and light Higgs boson production in $\Upsilon(1s)$ decays,” *Phys. Lett. B* **251** (1990) 204–210.
- [27] **BaBar** Collaboration, B. Aubert *et al.*, “Search for Invisible Decays of a Light Scalar in Radiative Transitions $\Upsilon(3S) \rightarrow \gamma + A^0$,” in *34th International Conference on High Energy Physics*, 7, 2008. arXiv:0808.0017 [hep-ex].
- [28] J. D. Bjorken, S. Ecklund, W. R. Nelson, A. Abashian, C. Church, B. Lu, L. W. Mo, T. A. Nunamaker, and P. Rassmann, “Search for Neutral Metastable Penetrating Particles Produced in the SLAC Beam Dump,” *Phys. Rev. D* **38** (1988) 3375.
- [29] B. Döbrich, “Axion-like Particles from Primakov production in beam-dumps,” *CERN Proc.* **1** (2018) 253, arXiv:1708.05776 [hep-ph].
- [30] E. M. Riordan *et al.*, “A Search for Short Lived Axions in an Electron Beam Dump Experiment,” *Phys. Rev. Lett.* **59** (1987) 755.
- [31] C. Hearty *et al.*, “Search for the Anomalous Production of Single Photons in e^+e^- Annihilation at $\sqrt{s} = 29\text{-GeV}$,” *Phys. Rev. D* **39** (1989) 3207.
- [32] J. Jaeckel, E. Masso, J. Redondo, A. Ringwald, and F. Takahashi, “The Need for purely laboratory-based axion-like particle searches,” *Phys. Rev. D* **75** (2007) 013004, arXiv:hep-ph/0610203.
- [33] **ARIADNE** Collaboration, A. A. Geraci *et al.*, “Progress on the ARIADNE axion experiment,” *Springer Proc. Phys.* **211** (2018) 151–161, arXiv:1710.05413 [astro-ph.IM].
- [34] **CAST** Collaboration, M. Arik *et al.*, “New solar axion search using the CERN Axion Solar Telescope with ^4He filling,” *Phys. Rev. D* **92** no. 2, (2015) 021101, arXiv:1503.00610 [hep-ex].
- [35] **IAXO** Collaboration, E. Armengaud *et al.*, “Physics potential of the International Axion Observatory (IAXO),” *JCAP* **06** (2019) 047, arXiv:1904.09155 [hep-ph].
- [36] **XENON, (XENON Collaboration)**** Collaboration, E. Aprile *et al.*, “Search for Light Dark Matter in Low-Energy Ionization Signals from XENONnT,” *Phys. Rev. Lett.* **134** no. 16, (2025) 161004, arXiv:2411.15289 [hep-ex].
- [37] **PandaX** Collaboration, T. Li *et al.*, “Search for MeV-Scale Axionlike Particles and Dark Photons with PandaX-4T,” *Phys. Rev. Lett.* **134** no. 7, (2025) 071004, arXiv:2409.00773 [hep-ex].
- [38] **LZ** Collaboration, J. Aalbers *et al.*, “Search for new physics in low-energy electron recoils from the first LZ exposure,” *Phys. Rev. D* **108** no. 7, (2023) 072006, arXiv:2307.15753 [hep-ex].
- [39] A. Berlin, S. Gori, P. Schuster, and N. Toro, “Dark Sectors at the Fermilab SeaQuest Experiment,” *Phys. Rev. D* **98** no. 3, (2018) 035011, arXiv:1804.00661 [hep-ph].
- [40] J. P. Chou, D. Curtin, and H. J. Lubatti, “New Detectors to Explore the Lifetime Frontier,” *Phys. Lett. B* **767** (2017) 29–36, arXiv:1606.06298 [hep-ph].
- [41] **CODEX-b** Collaboration, G. Aielli *et al.*, “Expression of interest for the CODEX-b detector,” *Eur. Phys. J. C* **80** no. 12, (2020) 1177, arXiv:1911.00481 [hep-ex].
- [42] J. L. Feng, I. Galon, F. Kling, and S. Trojanowski, “Forward Search Experiment at the LHC,” *Phys. Rev. D* **97** no. 3, (2018) 035001, arXiv:1708.09389 [hep-ph].
- [43] **SHiP** Collaboration, M. Anelli *et al.*, “A facility to Search for Hidden Particles (SHiP) at the CERN SPS,” arXiv:1504.04956 [physics.ins-det].
- [44] J. B. Dent, B. Dutta, D. Kim, S. Liao, R. Mahapatra, K. Sinha, and A. Thompson, “New Directions for Axion Searches via Scattering at Reactor Neutrino Experiments,” *Phys. Rev. Lett.* **124** no. 21, (2020) 211804, arXiv:1912.05733 [hep-ph].
- [45] D. Aristizabal Sierra, V. De Romeri, L. J. Flores, and D. K. Papoulias, “Axionlike particles searches in reactor experiments,” *JHEP* **03** (2021) 294, arXiv:2010.15712 [hep-ph].
- [46] F. Arias-Aragón, V. Brdar, and J. Quevillon, “New Directions for Axionlike Particle Searches Combining Nuclear Reactors and Haloscopes,” *Phys. Rev. Lett.* **132** no. 21, (2024) 211802, arXiv:2310.03631 [hep-ph].
- [47] C. Baruch, P. J. Fitzpatrick, T. Menzo, Y. Soreq, S. Trifinopoulos, and J. Zupan, “Searching for exotic scalars at fusion reactors,” arXiv:2502.12314 [hep-ph].
- [48] **CONNIE** Collaboration, A. Aguilar-Arevalo *et al.*, “The CONNIE experiment,” *J. Phys. Conf. Ser.* **761** no. 1, (2016) 012057, arXiv:1608.01565 [physics.ins-det].
- [49] **MINER** Collaboration, G. Agnolet *et al.*, “Background Studies for the MINER Coherent Neutrino Scattering Reactor Experiment,” *Nucl. Instrum. Meth. A* **853** (2017) 53–60, arXiv:1609.02066 [physics.ins-det].
- [50] **CONUS+** Collaboration, N. Ackermann *et al.*, “CONUS+ Experiment,” *Eur. Phys. J. C* **84** no. 12, (2024) 1265, arXiv:2407.11912 [hep-ex]. [Erratum: *Eur.Phys.J.C* **85**, 19 (2025)].
- [51] **JUNO** Collaboration, F. An *et al.*, “Neutrino Physics with JUNO,” *J. Phys. G* **43** no. 3, (2016) 030401, arXiv:1507.05613 [physics.ins-det].
- [52] **JUNO** Collaboration, A. Abusleme *et al.*, “JUNO physics and detector,” *Prog. Part. Nucl. Phys.* **123** (2022) 103927, arXiv:2104.02565 [hep-ex].
- [53] **JUNO** Collaboration, A. Abusleme *et al.*, “TAO Conceptual Design Report: A Precision Measurement of the Reactor Antineutrino Spectrum with Sub-percent Energy Resolution,” arXiv:2005.08745 [physics.ins-det].
- [54] M. Smirnov, G. Yang, J. Liao, Z. Hu, and J. Ling, “Light dark bosons in the JUNO-TAO neutrino detector,” *Phys. Rev. D* **104** no. 11, (2021) 116024, arXiv:2109.04276 [hep-ex].
- [55] **NEON** Collaboration, B. J. Park *et al.*, “New Constraints on Axionlike Particles with the NEON Detector at a Nuclear Reactor,” *Phys. Rev. Lett.* **134** no. 20, (2025) 201002, arXiv:2406.06117 [hep-ex].
- [56] M. Mirzakhani *et al.*, “MINER Reactor Based Search for Axion-Like Particles Using Sapphire (Al₂O₃) Detectors,” arXiv:2504.20960 [hep-ex].
- [57] **CLOUD** Collaboration, D. Navas Nicolas, “CLOUD: the First Reactor Antineutrino Experiment using the Novel LiquidO Detection Technology,” *PoS ICHEP2024* (2025) 157.
- [58] International Atomic Energy Agency, “IAEA,” 2025.

- https://nds.iaea.org/relnsd/vcharthtml/api_v0_guide.html. Livechart Data Download API.
- [59] D. Aloni, C. Fanelli, Y. Soreq, and M. Williams, “Photoproduction of Axionlike Particles,” *Phys. Rev. Lett.* **123** no. 7, (2019) 071801, arXiv:1903.03586 [hep-ph].
- [60] H. Bechteler, H. Faissner, R. Yogeshwar, and H. Seyfarth, “The Spectrum of γ Radiation Emitted in the FRJ-1 (Merlin) Reactor Core and Moderator Region,”
- [61] National Institute of Standard and Technologies, “NIST,” 2025. <https://physics.nist.gov/PhysRefData/Xcom/html/xcom1.html>. Photon Cross section database.
- [62] S. J. Brodsky, E. Mottola, I. J. Muzinich, and M. Soldate, “LASER INDUCED AXION PHOTOPRODUCTION,” *Phys. Rev. Lett.* **56** (1986) 1763. [Erratum: Phys.Rev.Lett. 57, 502 (1986)].
- [63] R. Chanda, J. F. Nieves, and P. B. Pal, “Astrophysical Constraints on Axion and Majoron Couplings,” *Phys. Rev. D* **37** (1988) 2714.
- [64] F. T. Avignone, C. Baktash, W. C. Barker, F. P. Calaprice, R. W. Dunford, W. C. Haxton, D. Kahana, R. T. Kouzes, H. S. Miley, and D. M. Moltz, “Search for Axions From the 1115-keV Transition of ^{65}Cu ,” *Phys. Rev. D* **37** (1988) 618–630.
- [65] SuperCDMS Collaboration, T. Aralis *et al.*, “Constraints on dark photons and axionlike particles from the SuperCDMS Soudan experiment,” *Phys. Rev. D* **101** no. 5, (2020) 052008, arXiv:1911.11905 [hep-ex]. [Erratum: Phys.Rev.D 103, 039901 (2021)].
- [66] X. Qian and J.-C. Peng, “Physics with Reactor Neutrinos,” *Rept. Prog. Phys.* **82** no. 3, (2019) 036201, arXiv:1801.05386 [hep-ex].
- [67] JUNO Collaboration, H. T. J. Steiger, “TAO—The Taishan Antineutrino Observatory,” *Instruments* **6** no. 4, (2022) 50.
- [68] Daya Bay Collaboration, F. P. An *et al.*, “A side-by-side comparison of Daya Bay antineutrino detectors,” *Nucl. Instrum. Meth. A* **685** (2012) 78–97, arXiv:1202.6181 [physics.ins-det].
- [69] RENO Collaboration, J. K. Ahn *et al.*, “RENO: An Experiment for Neutrino Oscillation Parameter θ_{13} Using Reactor Neutrinos at Yonggwang,” arXiv:1003.1391 [hep-ex].
- [70] G. Adhikari *et al.*, “Initial Performance of the COSINE-100 Experiment,” *Eur. Phys. J. C* **78** no. 2, (2018) 107, arXiv:1710.05299 [physics.ins-det].
- [71] National Nuclear Data Center Brookhaven National Laboratory, “NuDat (Nuclear Structure and Decay Data),” 2025. <https://www.nndc.bnl.gov/nudat3/>.
- [72] J. B. Birks, “Scintillations from Organic Crystals: Specific Fluorescence and Relative Response to Different Radiations,” *Proc. Phys. Soc. A* **64** (1951) 874–877.
- [73] C. Grupen and B. Schwartz, *Particle Detectors, Second Edition*. Cambridge University Press, 2008.
- [74] National Institute of Standard and Technologies, “NIST,” 2025. <https://physics.nist.gov/PhysRefData/Star/Text/ASTAR.html>.
- [75] H. Xu *et al.*, “Calibration strategy of the JUNO-TAO experiment,” *Eur. Phys. J. C* **82** no. 12, (2022) 1112, arXiv:2204.03256 [physics.ins-det].
- [76] I. S. Yeo *et al.*, “Measurement of the refractive index of the LAB-based liquid scintillator and acrylic at RENO,” *Phys. Scripta* **82** (2010) 065706.
- [77] P. Lombardi, F. Ortica, G. Ranucci, and A. Romani, “Decay time and pulse shape discrimination of liquid scintillators based on novel solvents,” *Nucl. Instrum. Meth. A* **701** (2013) 133–144.
- [78] National Institute of Standard and Technologies, “NIST,” 2025. <https://srdata.nist.gov/xps/SpectralByElm/C>. NIST X-ray Photoelectron Spectroscopy Database.
- [79] J. Berkowitz, *Photoabsorption, Photoionization, and Photoelectron Spectroscopy*. Academic Press, first ed., 1979.
- [80] D. C. Haynes, M. Wurzer, *et al.*, “Clocking Auger electrons,” *Nature Physics* **17** no. 4, (Jan., 2021) 512–518. <http://dx.doi.org/10.1038/s41567-020-01111-0>.
- [81] CAST Collaboration, E. Arik *et al.*, “Probing eV-scale axions with CAST,” *JCAP* **02** (2009) 008, arXiv:0810.4482 [hep-ex].
- [82] M. Minowa, S. Moriyama, Y. Inoue, T. Namba, Y. Takasu, and A. Yamamoto, “The Tokyo axion helioscope experiment,” *Nucl. Phys. B Proc. Suppl.* **72** (1999) 171–175, arXiv:hep-ex/9806015.
- [83] EDELWEISS Collaboration, E. Armengaud *et al.*, “Searches for electron interactions induced by new physics in the EDELWEISS-III Germanium bolometers,” *Phys. Rev. D* **98** no. 8, (2018) 082004, arXiv:1808.02340 [hep-ex].
- [84] R. Essig, R. Harnik, J. Kaplan, and N. Toro, “Discovering New Light States at Neutrino Experiments,” *Phys. Rev. D* **82** (2010) 113008, arXiv:1008.0636 [hep-ph].